Dynamic Impact of Zero-Sequence Circulating Current on Modular Multilevel Converters: Complex-Valued AC Impedance Modeling and Analysis

Wu, Heng; Wang, Xiongfei

Published in:
I E E E Journal of Emerging and Selected Topics in Power Electronics

DOI (link to publication from Publisher):
10.1109/JESTPE.2019.2951446

Publication date:
2020

Document Version
Publisher's PDF, also known as Version of record

Dynamic Impact of Zero-Sequence Circulating Current on Modular Multilevel Converters: Complex-Valued AC Impedance Modeling and Analysis

Heng Wu, *Student Member, IEEE*, and Xiongfei Wang, *Senior Member, IEEE*

***Abstract*— The stability impacts of the internal control dynamics of the modular multilevel converters (MMCs) have been discussed recently. Yet, the impact of zero-sequence circulating-current (ZSCC) dynamics on the ac-side dynamics of the MMCs is hitherto unaddressed. This article develops the ac impedance model for the grid-connected MMCs by means of complex vectors and harmonic transfer-function matrices, which allows separately characterizing the dynamics of the ZSCC. Then, based on the complex-valued model, a single-input–single-output closed-loop equivalent impedance is derived for grid-connected MMCs, considering both the frequency-coupling dynamics of the MMCs and the interactions with the grid impedance, which enables a design-oriented analysis on the stability impact of the ZSCC. It is revealed that the resonant peaks in the ac impedance of the MMC are yielded due to the absence of the ZSCC control, which tends to destabilize the system in weak grids. A systematic parameter-tuning method of the ZSCC control loop is developed to guarantee the system stability. Case studies in time-domain simulations corroborate the theoretical analysis.**

***Index Terms*— Circulating-current-suppression control (CCSC), complex vectors, impedance modeling, modular multilevel converters (MMCs), stability.**

I. Introduction

MODULAR multilevel converters (MMCs) are increasingly employed for high-voltage direct-current (HVDC) transmission systems, thanks to the advantages of modularity, scalability, and power controllability. Nevertheless, the modeling, stability analysis, and control of the MMCs are more complex than the conventional two-level voltage-source converters, due to their internal dynamics, i.e., the capacitor voltage variations of submodules [1].

The uncontrolled internal dynamics of the MMC bring in two major problems that deteriorate its efficient and reliable operation. One issue is the steady-state second-order-harmonic circulating current of the MMC [2], which increases the root-mean-square (rms) value of the arm currents and the total power loss. The other problem is multiple resonant peaks introduced in both the ac- and dc-side closed-loop output impedance of the MMC [3], [4], which may destabilize the MMC system. Hence, the circulating-current-suppression control (CCSC) is generally employed to address these challenges introduced by the internal dynamics of the MMCs [2]–[4].

There are two basic implementations of the CCSC for attenuating the second-order-harmonic circulating current. The first scheme is using the proportional integral (PI) regulator in the dq frame, which rotates at the double-line frequency [2], and the second method is using the proportional-resonant (PR) regulator with the fixed double-line resonant frequency in the $\alpha\beta$ frame [5]. However, in both cases, the zero-sequence circulating currents (ZSCCs), which are the three-phase ac components of the circulating currents with the same magnitudes and phase angles [5], are omitted during the abc to $dq0$ or abc to $\alpha\beta0$ transformation and left uncontrolled. This is due to the fact that the steady-state second-order-harmonic circulating current merely emerges as the negative sequence component during the normal operation of MMCs in three-phase balanced power systems [2].

The dynamic impact of the CCSC on the small-signal stability of the MMCs has recently been discussed. It is shown in [3] and [6]–[8] that the proportional gain of the CCSC is equivalent to the virtual arm resistor, which provides additional damping to the dynamics of the MMCs. However, even if the basic CCSC is adopted, a poorly damped dc-side dynamics of the MMC is still yielded when the ZSCC control is unused [4], [9], [10]. While the steady-state ZSCC is absent in three-phase balanced MMC systems, the poorly damped dc-side dynamics can interact with the parasitic capacitance of dc power transmission cables, leading to the oscillating ZSCC within MMCs. It is worth noting that such an oscillating ZSCC implies the unstable operation of the system, and is thus different from the steady-state second-order ZSCC introduced by the three-phase unbalanced grid voltages [5], [11], [12]. Therefore, to mitigate the dc-side oscillations, the ZSCC control is recommended even under three-phase balanced power systems [4], [9], [10]. Nevertheless, the studies in [4], [9], and [10] assume a stiff ac balanced grid for the MMC. The impact of the ZSCC control

Manuscript received June 26, 2019; revised September 18, 2019; accepted October 24, 2019. Date of publication November 5, 2019; date of current version May 6, 2020. This work was supported in part by the Aalborg University Strategic Talent Management Programme and in part by TenneT TSO GmbH. Recommended for publication by Associate Editor Margarita Norambuena. *(Corresponding author: Xiongfei Wang.)*

The authors are with the Department of Energy Technology, Aalborg University, 9220 Aalborg, Denmark (e-mail: hew@et.aau.dk; xwa@et.aau.dk).

Color versions of one or more of the figures in this article are available online at http://ieeexplore.ieee.org.

Digital Object Identifier 10.1109/JESTPE.2019.2951446

on the ac-side dynamics of MMCs and its interaction with the ac grid impedance are overlooked. Due to the coupling between the internal and external dynamics of the MMCs, not only the dc-side dynamics but also the ac-side dynamics of the MMC can induce the oscillating ZSCC even under the three-phase balanced grid.

This article attempts to close this gap by developing a complex-valued impedance model for the MMC with three-phase balanced grid voltages. The complex-valued impedance model is based on complex vectors and harmonic transfer-function (HTF) matrices, which differs from the conventional small-signal models reported in [13]–[18]. The conventional impedance models are represented by real vectors, e.g., *abc* three-phase variables, where the sequence components are hidden in each phase quantity and, consequently, the dynamic impact of the ZSCC is hardly revealed. In contrast, with the help of complex vectors, the dynamics of the sequence components can be explicitly captured, and thus, the ZSCC dynamics can be separately investigated.

Furthermore, since the obtained impedance model is multiple-input multiple-output (MIMO), which hardly provides a design-oriented analysis [19], [20], a single-input–single-output (SISO) equivalent ac impedance model of the grid-connected MMC, considering its frequency-coupling dynamics and interaction with the grid impedance, is further derived with the complex-vector representation. Thus, the SISO Nyquist stability criterion can be readily applied to the stability analysis. Based on the SISO equivalent impedance model, a comparison between the ac-side impedance of the MMC with and without the ZSCC control is presented. It is revealed that resonant peaks in the ac equivalent impedance of the MMC are yielded due to the absence of the ZSCC control, which can lead to ac-side oscillations when the MMC is connected with weak ac grids. In contrast, these resonant peaks can be effectively damped by the ZSCC control and a stable operation of the MMC can be guaranteed. These findings complement the dc-side dynamic analysis in [4], [9], and [10], implying that the ZSCC control plays a critical role in stabilizing both the dc- and ac-side dynamics of the MMC, and is thus recommended to be implemented in the CCSC even in the three-phase balanced power systems. A systematic parameter-tuning guideline for the ZSCC control loop is finally proposed. The correctness of the theoretical analysis is validated by case studies in electromagnetic transient simulations.

II. Small-Signal Modeling of the Power Stage of the MMC

Fig. 1(a) shows a single-phase circuit diagram of the three-phase three-wire MMC, and its arm-averaged model is given in Fig. 1(b) (see [13]–[18]). In the MMC, each arm has N submodules connected in series. C represents the capacitor of each submodule. $v_{ui}(i = a, b, c)$, v_{li}, i_{ui}, i_{li}, v_{cui}, v_{cli}, $v_{cui\Sigma}$, $v_{cli\Sigma}$, m_{ui}, and m_{li} are the arm voltages, the arm currents, the submodule capacitor voltages, the sum of the submodule capacitor voltages, and the control signals for the upper and lower arms of the MMC, respectively. $v_{\mathrm{ac}i}$ and $i_{\mathrm{ac}i}$ are the ac output voltage and current, respectively. N_1 represents the neutral point of the ac terminal, while O represents the middle point of the dc terminal.

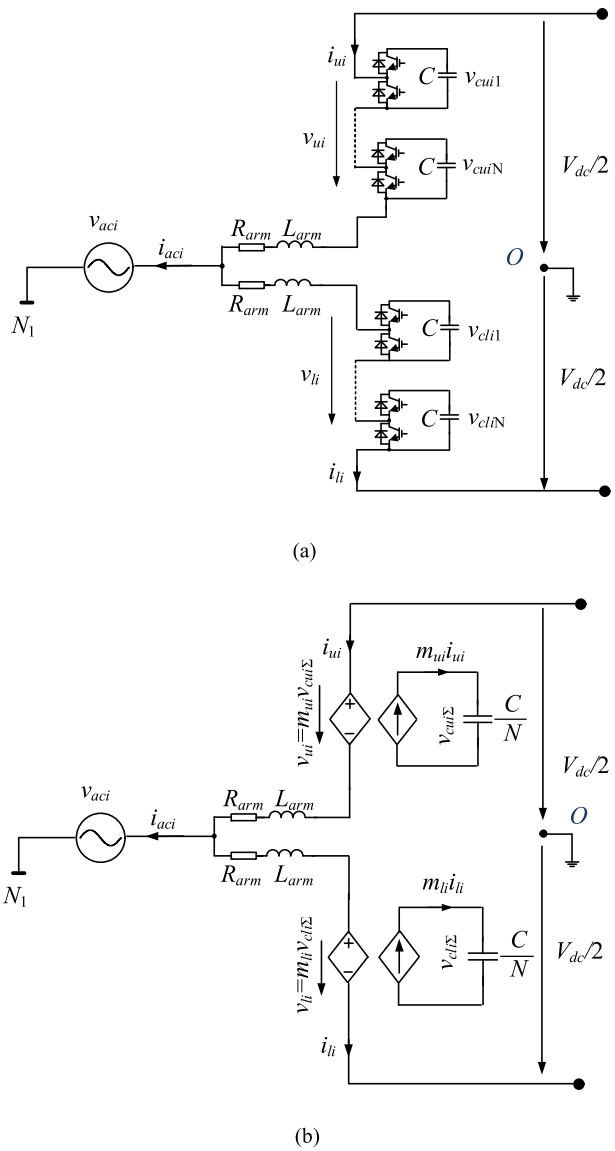

Fig. 1. Single-phase diagram of the three-phase–three-wire MMC. (a) Detailed circuit model. (b) Arm averaged model.

Since the focus of this article is the impact of the ZSCC control on the ac-side dynamics of the MMC, rather than the dc-side dynamics that has been reported in [4], [9], and [10], the dc-side voltage V_{dc} is assumed constant in this article. As will be demonstrated in the following, even if the destabilization due to the dc-side dynamic interaction described in [4], [9], and [10] is manually avoided, the risk of the instability persists when the MMC is connected to the weak ac grid, provided its ZSCC is not properly controlled.

Applying Kirchhoff's law to the upper and lower arms of the MMC yields

$$\frac{V_{\mathrm{dc}}}{2} - m_{ui}v_{cui\Sigma} - v_{\mathrm{ac}i} - v_{N_1O} = L_{\mathrm{arm}}\frac{di_{ui}}{dt} + R_{\mathrm{arm}}i_{ui} \tag{1}$$

$$v_{N_1O} + v_{\mathrm{ac}i} - \left(-\frac{V_{\mathrm{dc}}}{2} + m_{li}v_{cli\Sigma}\right) = L_{\mathrm{arm}}\frac{di_{li}}{dt} + R_{\mathrm{arm}}i_{li} \tag{2}$$

where v_{N_1O} is the voltage difference between the point N_1 and the point O.

The internal dynamics of the MMC can be expressed as [6]

$$\frac{C}{N}\frac{dv_{cui\sum}}{dt} = m_{ui}i_{ui}, \quad \frac{C}{N}\frac{dv_{cli\sum}}{dt} = m_{li}i_{li}. \tag{3}$$

Define the ac output current and the circulating current as $i_{\mathrm{aci}} = i_{ui} - i_{li}$, $i_{\mathrm{ciri}} = (i_{ui} + i_{li})/2$, the ac- and dc-side control signals of the MMC as $m_{\mathrm{aci}} = (m_{li} - m_{ui})/2$, $m_{\mathrm{dci}} = m_{ui} + m_{li}$, and the sum and difference of the capacitor voltages of the upper and lower arms as $v_{ci\Sigma} = v_{cui\Sigma} + v_{cli\Sigma}$ and $v_{ci\Delta} = v_{cui\Sigma} - v_{cli\Sigma}$. Then, (1)–(3) can be rewritten as

$$\frac{m_{\mathrm{aci}}v_{ci\sum}}{2} - \frac{m_{\mathrm{dci}}v_{ci\Delta}}{4} - v_{\mathrm{aci}} - v_{N_1O} = \frac{L_{\mathrm{arm}}}{2}\frac{di_{\mathrm{aci}}}{dt} + \frac{R_{\mathrm{arm}}}{2}i_{\mathrm{aci}} \tag{4}$$

$$v_{\mathrm{dc}} - \left(\frac{m_{\mathrm{dci}}}{2}v_{ci\sum} - m_{\mathrm{aci}}v_{ci\Delta}\right) = 2L_{\mathrm{arm}}\frac{di_{ciri}}{dt} + 2R_{\mathrm{arm}}i_{ciri} \tag{5}$$

$$C\frac{dv_{ci\sum}}{dt} = N\left(m_{\mathrm{dci}}i_{ciri} - m_{\mathrm{aci}}i_{\mathrm{aci}}\right) \tag{6}$$

$$C\frac{dv_{ci\Delta}}{dt} = N\left(\frac{m_{\mathrm{dci}}i_{\mathrm{aci}}}{2} - 2m_{\mathrm{aci}}i_{ciri}\right). \tag{7}$$

Defining that

$$v_{\mathrm{acMMC}i} = \frac{m_{\mathrm{aci}}v_{ci\sum}}{2} - \frac{m_{\mathrm{dci}}v_{ci\Delta}}{4} \tag{8}$$

then, v_{N_1O} can be expressed as [14]

$$v_{N_1O} = \frac{v_{\mathrm{acMMC}a} + v_{\mathrm{acMMC}b} + v_{\mathrm{acMMC}c}}{3}. \tag{9}$$

Equations (4)–(9) represent the dynamics of the power stage of the MMC [6]. It is noted that all state variables in (4)–(9) are periodic signals in the steady state, and hence, the MMC is essentially a nonlinear time-periodic (NTP) system.

The small-signal linear time-periodic (LTP) equations of the MMC can be then obtained by linearizing (4)–(9) around its operation trajectories, which are expressed as [13]

$$\frac{d\hat{i}_{\mathrm{aci}}}{dt} = -\frac{2}{L_{\mathrm{arm}}}\hat{v}_{\mathrm{aci}} - \frac{R_{\mathrm{arm}}}{L_{\mathrm{arm}}}\hat{i}_{\mathrm{aci}} + \frac{M_{\mathrm{aci}}(t)\hat{v}_{ci\sum} + V_{ci\sum}(t)\hat{m}_{\mathrm{aci}}}{L_{\mathrm{arm}}} - \frac{M_{\mathrm{dci}}(t)\hat{v}_{ci\Delta} + V_{ci\Delta}(t)\hat{m}_{\mathrm{dci}}}{2L_{\mathrm{arm}}} - \hat{v}_{N_1O} \tag{10}$$

$$\frac{d\hat{i}_{ciri}}{dt} = \frac{1}{2L_{\mathrm{arm}}}\hat{v}_{\mathrm{dc}} - \frac{R_{\mathrm{arm}}}{L_{\mathrm{arm}}}\hat{i}_{ciri} - \frac{M_{\mathrm{dci}}(t)\hat{v}_{ci\sum} + V_{ci\sum}(t)\hat{m}_{\mathrm{dci}}}{4L_{\mathrm{arm}}} + \frac{M_{\mathrm{aci}}(t)\hat{v}_{ci\Delta} + V_{ci\Delta}(t)\hat{m}_{\mathrm{aci}}}{2L_{\mathrm{arm}}} \tag{11}$$

$$\frac{d\hat{v}_{ci\sum}}{dt} = \frac{N}{C}[M_{\mathrm{dci}}(t)\hat{i}_{ciri} + I_{ciri}(t)\hat{m}_{\mathrm{dci}}] - \frac{N}{C}[M_{\mathrm{aci}}(t)\hat{i}_{\mathrm{aci}} + I_{\mathrm{aci}}(t)\hat{m}_{\mathrm{aci}}] \tag{12}$$

$$\frac{d\hat{v}_{ci\Delta}}{dt} = \frac{N}{2C}[M_{\mathrm{dci}}(t)\hat{i}_{\mathrm{aci}} + I_{\mathrm{aci}}(t)\hat{m}_{\mathrm{dci}}] - \frac{2N}{C}[M_{\mathrm{aci}}(t)\hat{i}_{ciri} + I_{ciri}(t)\hat{m}_{\mathrm{aci}}] \tag{13}$$

$$\hat{v}_{N_1O} = \frac{M_{\mathrm{aca}}(t)\hat{v}_{ca\sum} + V_{ca\sum}(t)\hat{m}_{\mathrm{aca}}}{6} - \frac{M_{\mathrm{dca}}(t)\hat{v}_{ca\Delta} + V_{ca\Delta}(t)\hat{m}_{\mathrm{dca}}}{12} + \frac{M_{\mathrm{acb}}(t)\hat{v}_{cb\sum} + V_{cb\sum}(t)\hat{m}_{\mathrm{acb}}}{6} - \frac{M_{\mathrm{dcb}}(t)\hat{v}_{cb\Delta} + V_{cb\Delta}(t)\hat{m}_{\mathrm{dcb}}}{12} + \frac{M_{\mathrm{acc}}(t)\hat{v}_{cc\sum} + V_{cc\sum}(t)\hat{m}_{\mathrm{acc}}}{6} - \frac{M_{\mathrm{dcc}}(t)\hat{v}_{cc\Delta} + V_{cc\Delta}(t)\hat{m}_{\mathrm{dcc}}}{12}. \tag{14}$$

Rewriting (10)–(14) in the matrix form, which yields

$$\dot{\hat{\mathbf{x}}}_{\mathbf{abc}}(\mathbf{t}) = \mathbf{A}_{\mathbf{abc}}(\mathbf{t})\,\hat{\mathbf{x}}_{\mathbf{abc}}(\mathbf{t}) + \mathbf{B}_{\mathbf{abc}}(\mathbf{t})\hat{\mathbf{u}}_{\mathbf{abc}}(\mathbf{t}) \tag{15}$$

where

$$\hat{\mathbf{x}}_{\mathbf{abc}}(\mathbf{t}) = \left[\hat{i}_{\mathrm{ac}abc}(t), \hat{i}_{cirabc}(t), \hat{v}_{c\sum abc}(t), \hat{v}_{c\Delta abc}(t)\right]^T$$
$$\hat{\mathbf{u}}_{\mathbf{abc}}(\mathbf{t}) = \left[\hat{m}_{\mathrm{ac}abc}(t), \hat{m}_{\mathrm{dc}abc}(t), \hat{v}_{\mathrm{ac}abc}(t), \hat{v}_{\mathrm{dc}abc}(t)\right]^T \tag{16}$$

and $\mathbf{A}_{\mathbf{abc}}(\mathbf{t})$ and $\mathbf{B}_{\mathbf{abc}}(\mathbf{t})$ are given in Appendix A.

It is clear that the model given by (15) is based on real vectors (*abc* three-phase variables). With the basic sequence transformation [21], the real-vector-based model can be transformed into its complex equivalent form represented by complex vectors, which are given by

$$\begin{bmatrix} x_{\alpha\beta+} \\ x_{\alpha\beta-} \\ x_{\alpha\beta0} \end{bmatrix} = T_1\begin{bmatrix} x_\alpha \\ x_\beta \\ x_0 \end{bmatrix} = T_1T_2\begin{bmatrix} x_a \\ x_b \\ x_c \end{bmatrix} \tag{17}$$

$$T_1 = \begin{pmatrix} 1 & j & \\ 1 & -j & \\ & & 1 \end{pmatrix} \quad T_2 = \begin{pmatrix} \frac{2}{3} & -\frac{1}{3} & -\frac{1}{3} \\ 0 & \frac{\sqrt{3}}{3} & -\frac{\sqrt{3}}{3} \\ \frac{1}{3} & \frac{1}{3} & \frac{1}{3} \end{pmatrix} \tag{18}$$

where $x_{\alpha\beta+}$, $x_{\alpha\beta-}$, and $x_{\alpha\beta0}$ are the complex vectors of the three-phase variables (x_a, x_b, and x_c), respectively. In general, the frequency of $x_{\alpha\beta+}$, $x_{\alpha\beta-}$, and $x_{\alpha\beta0}$ ranges from $-\infty$ to $+\infty$ in the dynamic analysis. $x_{\alpha\beta+}(x_{\alpha\beta-})$ represents the positive- (negative-) sequence component in the positive frequency range and the negative- (positive-) sequence component in the negative frequency range. Yet, $x_{\alpha\beta0}$ always represents the zero-sequence component [21].

It is noted that the transformation given in (17) is for one group of three-phase variables, it is known from (16) that there are four different groups of three-phase variables in $\hat{\mathbf{x}}_{\mathbf{abc}}$ and $\hat{\mathbf{u}}_{\mathbf{abc}}$, and thus, the transformation matrix used here is

$$\mathbf{P} = \mathrm{diag}[T_1T_2,\ T_1T_2,\ T_1T_2,\ T_1T_2]. \tag{19}$$

Then, (15) can be transformed with the complex-vector representation, which is expressed as

$$\begin{aligned}\mathbf{P^{-1}}\dot{\hat{\mathbf{x}}}_{\boldsymbol{\alpha\beta}+-0}(\mathbf{t}) &= \mathbf{A_{abc}}(\mathbf{t})[\mathbf{P^{-1}}\hat{\mathbf{x}}_{\boldsymbol{\alpha\beta}+-0}(\mathbf{t})] \\ &\quad +\mathbf{B_{abc}}(\mathbf{t})[\mathbf{P^{-1}}\hat{\mathbf{u}}_{\boldsymbol{\alpha\beta}+-0}(\mathbf{t})] \\ &\Leftrightarrow \dot{\hat{\mathbf{x}}}_{\boldsymbol{\alpha\beta}+-0}(\mathbf{t}) = [\mathbf{PA_{abc}}(\mathbf{t})\mathbf{P^{-1}}]\hat{\mathbf{x}}_{\boldsymbol{\alpha\beta}+-0}(\mathbf{t}) \\ &\quad +[\mathbf{PB_{abc}}(\mathbf{t})\mathbf{P^{-1}}]\hat{\mathbf{u}}_{\boldsymbol{\alpha\beta}+-0}(\mathbf{t}) \end{aligned} \tag{20}$$

which characterizes the LTP dynamics of the power stage of the MMC in the time domain, and its corresponding linear time-invariant (LTI) representation in the frequency domain can be derived based on the harmonic state-space (HSS) method [22]. The detailed modeling procedure is elaborated in Appendix B, and only the results are given below

$$s\hat{\mathbf{x}}_{\boldsymbol{\alpha\beta}+-0} = \mathbf{A_{hss\alpha\beta}}_{+-0}\hat{\mathbf{x}}_{\boldsymbol{\alpha\beta}+-0}+\mathbf{B_{hss\alpha\beta}}_{+-0}\hat{\mathbf{u}}_{\boldsymbol{\alpha\beta}+-0} \tag{21}$$

$$\hat{\mathbf{x}}_{\boldsymbol{\alpha\beta}+-0} = \begin{bmatrix} \hat{X}_{-h} \\ \vdots \\ \hat{X}_{-1} \\ \hat{X}_0 \\ \hat{X}_1 \\ \vdots \\ \hat{X}_h \end{bmatrix}, \quad \hat{X}_h = \begin{bmatrix} \hat{i}_{\mathrm{ac}\alpha\beta+-0}\,(s+jh\omega_0) \\ \hat{i}_{cir\alpha\beta+-0}\,(s+jh\omega_0) \\ \hat{v}_{c\sum\alpha\beta+-0}\,(s+jh\omega_0) \\ \hat{v}_{c\Delta\alpha\beta+-0}\,(s+jh\omega_0) \end{bmatrix} \tag{22}$$

$$\hat{\mathbf{u}}_{\boldsymbol{\alpha\beta}+-0} = \begin{bmatrix} \hat{U}_{-h} \\ \vdots \\ \hat{U}_{-1} \\ \hat{U}_0 \\ \hat{U}_1 \\ \vdots \\ \hat{U}_h \end{bmatrix}, \quad \hat{U}_h = \begin{bmatrix} \hat{m}_{\mathrm{ac}\alpha\beta+-0}\,(s+jh\omega_0) \\ \hat{m}_{\mathrm{dc}\alpha\beta+-0}\,(s+jh\omega_0) \\ \hat{v}_{\mathrm{ac}\alpha\beta+-0}\,(s+jh\omega_0) \\ \hat{v}_{\mathrm{dc}\alpha\beta+-0}\,(s+jh\omega_0) \end{bmatrix} \tag{23}$$

$$\mathbf{A_{hss\alpha\beta}}_{+-0} = \Gamma\left[\mathbf{PA_{abc}}(\mathbf{t})\mathbf{P^{-1}}\right] - \mathbf{N} \tag{24}$$

$$\mathbf{B_{hss\alpha\beta}}_{+-0} = \Gamma\left[\mathbf{PB_{abc}}(\mathbf{t})\mathbf{P^{-1}}\right] \tag{25}$$

where ω_0 is the fundamental frequency and h represents the harmonic order. $\mathbf{N}$ and $\mathbf{\Gamma}$ are the diagonal and Toeplitz matrices defined in (B.6) and (B.7) in Appendix B, respectively.

It is noted that (21) provides the universal power-stage model of the MMC, which considers the dynamics of all state variables. However, the constant dc voltage is assumed in this article, and thus, $\hat{v}_{\mathrm{dc}} = 0$ is adopted in the following analysis.

III. Small-Signal Modeling of the Closed-Loop-Controlled MMC

For the MMC with the closed-loop control, the control signals $\hat{m}_{\mathrm{ac}\alpha\beta+-0}(s+jh\omega_0)$ and $\hat{m}_{\mathrm{dc}\alpha\beta+-0}(s+jh\omega_0)$ in $\hat{\mathbf{u}}_{\boldsymbol{\alpha\beta}+-0}$ are determined by the control loops of the MMC. In order to facilitate the integration of the control-loop model into the power-stage model of the MMC, (21) is rewritten as

$$\begin{aligned}\mathbf{s\hat{x}}_{\boldsymbol{\alpha\beta}+-0} &= \mathbf{A_{hss\alpha\beta}}_{+-0}\hat{\mathbf{x}}_{\boldsymbol{\alpha\beta}+-0}+\mathbf{B_{mhss\alpha\beta}}_{+-0}\hat{\mathbf{m}}_{\boldsymbol{\alpha\beta}+-0} \\ &\quad +\mathbf{B_{vhss\alpha\beta}}_{+-0}\hat{\mathbf{v}}_{\boldsymbol{\alpha\beta}+-0} \end{aligned} \tag{26}$$

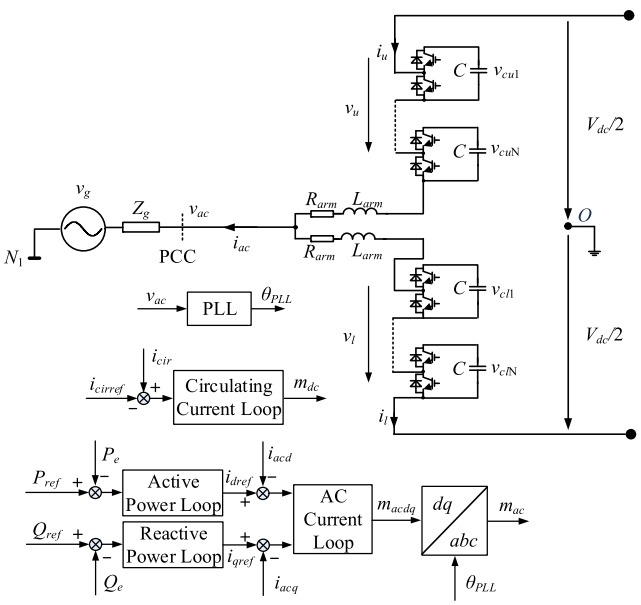

Fig. 2. Single-phase diagram of the MMC operated in the grid-connected mode with the closed-loop control.

where

$$\begin{aligned}\hat{\mathbf{m}}_{\boldsymbol{\alpha\beta}+-0} &= [\,\hat{M}_{-h}\ \cdots\ \hat{M}_{-1}\ \hat{M}_0\ \hat{M}_1\ \cdots\ \hat{M}_h\,]^T \\ \hat{M}_h &= [\,\hat{m}_{\mathrm{ac}\boldsymbol{\alpha\beta}+-0}(s+jh\omega_0)\ \hat{m}_{\mathrm{dc}\boldsymbol{\alpha\beta}+-0}(s+jh\omega_0)\,]^T \end{aligned} \tag{27}$$

$$\begin{aligned}\hat{\mathbf{v}}_{\boldsymbol{\alpha\beta}+-0} &= [\,\hat{V}_{-h}\ \cdots\ \hat{V}_{-1}\ \hat{V}_0\ \hat{V}_1\ \cdots\ \hat{V}_h\,]^T \\ \hat{V}_h &= [\,\hat{v}_{\mathrm{ac}\alpha\beta+-0}(s+jh\omega_0)\ \hat{v}_{\mathrm{dc}\alpha\beta+-0}(s+jh\omega_0)\,]^T \end{aligned} \tag{28}$$

and $\mathbf{B_{mhss\alpha\beta\pm0}}$ and $\mathbf{B_{vhss\alpha\beta\pm0}}$ are the submatrices of $\mathbf{B_{hss\alpha\beta\pm0}}$ in (25).

The dynamics of the control loops can be generally expressed as

$$\hat{\mathbf{m}}_{\boldsymbol{\alpha\beta}+-0} = \mathbf{G_x}\hat{\mathbf{x}}_{\boldsymbol{\alpha\beta}+-0}+\mathbf{G_v}\hat{\mathbf{v}}_{\boldsymbol{\alpha\beta}+-0} \tag{29}$$

where $\mathbf{G_x}$ and $\mathbf{G_v}$ are changed with different control schemes.

Substituting (29) into (26), the small-signal model of the closed-loop-controlled MMC can be obtained, which is given by

$$\begin{aligned}\mathbf{s\hat{x}}_{\boldsymbol{\alpha\beta}+-0} &= (\mathbf{A_{hss\alpha\beta}}_{+-0} + \mathbf{B_{mhss\alpha\beta}}_{+-0}\mathbf{G_x})\hat{\mathbf{x}}_{\boldsymbol{\alpha\beta}+-0} \\ &\quad +(\mathbf{B_{mhss\alpha\beta}}_{+-0}\mathbf{G_v} + \mathbf{B_{vhss\alpha\beta}}_{+-0})\hat{\mathbf{v}}_{\boldsymbol{\alpha\beta}+-0}. \end{aligned} \tag{30}$$

Fig. 2 shows the single-phase diagram of a three-phase grid-connected MMC with the closed-loop control system. Z_g is the grid impedance. The ac current loop is used to control the ac output current of the MMC, where the current references are generated by the active and reactive power control loops. The voltage at the point of the common coupling (PCC) is measured for synchronizing the MMC with the power grid by means of the phase-locked loop (PLL). The CCSC is adopted to suppress the second-order harmonic in the circulating current.

A. Circulating-Current Control

Fig. 3 shows the block diagram of the commonly used CCSC implemented in the $\alpha\beta$ frame [5]. $G_{\mathrm{delay}}(s)$ represents

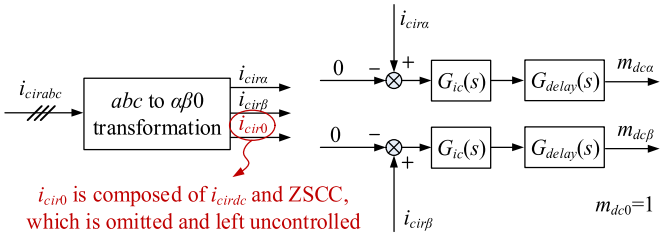

Fig. 3. Block diagram of the classical CCSC without controlling the ZSCC.

the control delay of the MMC. It is clear that the ZSCC is omitted through the *abc*–$\alpha\beta0$ transformation, and is thus left uncontrolled [5]. The PR controller with its resonant frequency tuned at $2\omega_0$ is used as the circulating-current regulator, which is expressed as

$$G_{\rm ic}(s) = K_{\rm Pic} + \frac{2K_{\rm Ric}\omega_i s}{s^2 + 2\omega_i s + (2\omega_0)^2} \tag{31}$$

where $K_{\rm Pic}$ and $K_{\rm Ric}$ are the proportional and resonant gains of the circulating-current regulator, respectively. The relationship between $\hat{m}_{{\rm dc}\alpha\beta0}$ and $\hat{i}_{cir\alpha\beta0}$ can thus be expressed as

$$\begin{aligned}\begin{bmatrix}\hat{m}_{{\rm dc}\alpha}(s)\\ \hat{m}_{{\rm dc}\beta}(s)\\ \hat{m}_{{\rm dc}0}(s)\end{bmatrix} &= \begin{bmatrix}G_{ic}(s)\,G_{\rm delay}(s) & & \\ & G_{ic}(s)\,G_{\rm delay}(s) & \\ & & 0\end{bmatrix}\begin{bmatrix}\hat{i}_{cir\alpha}(s)\\ \hat{i}_{cir\beta}(s)\\ \hat{i}_{cir0}(s)\end{bmatrix}\\ &\triangleq \mathbf{G_{tfcir}}\begin{bmatrix}\hat{i}_{cir\alpha}(s)\\ \hat{i}_{cir\beta}(s)\\ \hat{i}_{cir0}(s)\end{bmatrix}.\end{aligned} \tag{32}$$

Then, the corresponding complex-vector representation of (32) can be expressed as

$$\begin{bmatrix}\hat{m}_{{\rm dc}\alpha\beta+}(s)\\ \hat{m}_{{\rm dc}\alpha\beta-}(s)\\ \hat{m}_{{\rm dc}\alpha\beta0}(s)\end{bmatrix} = T_1\mathbf{G_{tfcir}}T_1^{-1}\begin{bmatrix}\hat{i}_{cir\alpha\beta+}(s)\\ \hat{i}_{cir\alpha\beta-}(s)\\ \hat{i}_{cir0}(s)\end{bmatrix}. \tag{33}$$

Fig. 4 shows the block diagram for the CCSC with the ZSCC control loop. Since the dc-side current of the MMC is the sum of three-phase circulating currents, the positive- and negative-sequence components of the circulating current cancel out with each other when adding up, and only the dc and zero-sequence components remain. Hence, the ZSCC has a significant impact on the dynamics of the dc-side current. Two methods of controlling the ZSCC are reported in [4], [9], and [10]. The first method is to control the dc and zero-sequence components of the circulating current to track its reference value, which is dictated by controlling the total energy stored in the MMC capacitors [9], as shown in Fig. 4(a), where $E_{\rm cref}$ and $E_{\rm cfb}$ represent the reference and feedback values of the total energy stored in the MMC capacitors, respectively. It is clear that an additional effort for tuning the outer energy controller is required in this method. The second approach is more straightforward, which directly uses the ZSCC for active

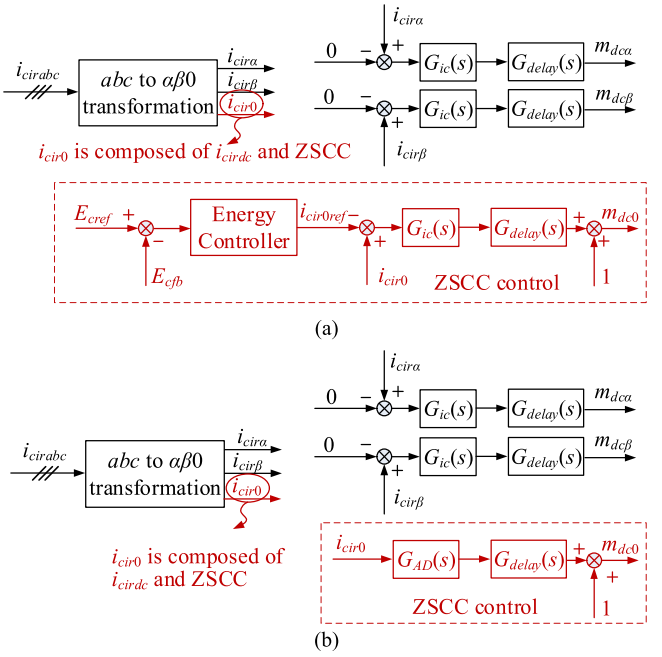

Fig. 4. Block diagram of the CCSC with the ZSCC control. (a) Energy-based ZSCC control [9]. (b) ZSCC-based active damping [4], [10].

damping [4], [10], as shown in Fig. 4(b). $G_{\rm AD}(s)$ is the transfer function of the damping controller, which is expressed as

$$G_{\rm AD}(s) = R_{\rm AD}\frac{s}{s+\omega_{\rm AD}} \tag{34}$$

where $R_{\rm AD}$ is the active damping resistor and $\omega_{\rm AD}$ is the crossover frequency of the high-pass filter. The high-pass filter is used to filter out the dc component of the circulating current. It should be emphasized again that the ZSCC control in [4], [9], and [10] is adopted for damping the dc-side oscillation of the MMC, and its impact on the ac-side dynamics of the MMC has not been addressed.

In this article, the control method shown in Fig. 4(b) is used as a benchmark to study the impact of the ZSCC control on the ac-side dynamics of the MMC.

Based on Fig. 4(b), the relationship between $\hat{m}_{{\rm dc}\alpha\beta0}$ and $\hat{i}_{cir\alpha\beta0}$ can be expressed as

$$\begin{aligned}\begin{bmatrix}\hat{m}_{{\rm dc}\alpha}(s)\\ \hat{m}_{{\rm dc}\beta}(s)\\ \hat{m}_{{\rm dc}0}(s)\end{bmatrix} &= \begin{bmatrix}G_{ic}(s)\,G_{\rm delay}(s) & & \\ & G_{ic}(s)\,G_{\rm delay}(s) & \\ & & G_{\rm AD}(s)\,G_{\rm delay}(s)\end{bmatrix}\\ &\quad\times\begin{bmatrix}\hat{i}_{cir\alpha}(s)\\ \hat{i}_{cir\beta}(s)\\ \hat{i}_{cir0}(s)\end{bmatrix}\\ &\triangleq \mathbf{G_{tfcirz}}\begin{bmatrix}\hat{i}_{cir\alpha}(s)\\ \hat{i}_{cir\beta}(s)\\ \hat{i}_{cir0}(s)\end{bmatrix}.\end{aligned} \tag{35}$$

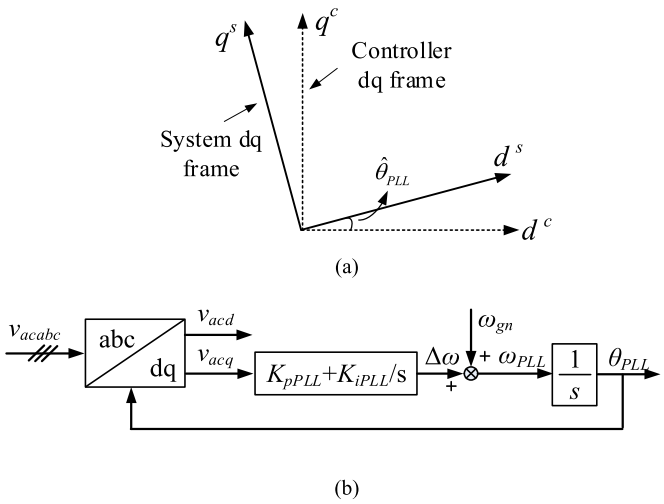

Fig. 5. Representation of the synchronization dynamics of the PLL. (a) Controller dq frame and system *dq* frame. (b) Block diagram of the PLL.

The corresponding complex-vector representation of (35) is given by

$$\begin{bmatrix} \hat{m}_{\mathrm{dc}\alpha\beta+}(s) \\ \hat{m}_{\mathrm{dc}\alpha\beta-}(s) \\ \hat{m}_{\mathrm{dc}\alpha\beta 0}(s) \end{bmatrix} = T_1 \mathbf{G_{tfcirz}} T_1^{-1} \begin{bmatrix} \hat{i}_{cir\alpha\beta+}(s) \\ \hat{i}_{cir\alpha\beta-}(s) \\ \hat{i}_{cir0}(s) \end{bmatrix}. \quad (36)$$

B. Active/Reactive Power Loop, AC Current Loop, and the PLL

It is known from Fig. 2 that the active/reactive power control and the ac current control are implemented in the rotating frame determined by the output phase of the PLL, which is defined as the controller-*dq* frame hereafter [23]. Another rotating frame with the phase angle of the grid voltage is defined as the system-*dq* frame [23]. Both frames are shown in Fig. 5(a). The deviation between the controller-*dq* frame and the system-*dq* frame is determined by the PLL dynamics.

In order to capture the dynamic effect of the PLL, the system model is finally derived in the system-*dq* frame [23]. The relationships between the state variables in the controller-*dq* frame ($\hat{x}^c_{dq+}$ and $\hat{x}^c_{dq-}$) and the system-*dq* frame ($\hat{x}^s_{dq+}$ and $\hat{x}^s_{dq-}$) are given by [23]

$$\begin{bmatrix} \hat{x}^c_{dq+} \\ \hat{x}^c_{dq-} \end{bmatrix} = \begin{bmatrix} \hat{x}^s_{dq+} \\ \hat{x}^s_{dq-} \end{bmatrix} - \frac{G_{\mathrm{PLL}}}{2} \begin{bmatrix} X^s_d + jX^s_q & -\left(X^s_d + jX^s_q\right) \\ -\left(X^s_d - jX^s_q\right) & X^s_d - jX^s_q \end{bmatrix} \times \begin{bmatrix} \hat{v}^s_{\mathrm{acd}dq+} \\ \hat{v}^s_{\mathrm{acd}dq-} \end{bmatrix} \quad (37)$$

$$G_{\mathrm{PLL}} = \frac{K_{p\mathrm{PLL}}s + K_{i\mathrm{PLL}}}{s^2 + V_{\mathrm{acd}}\left(K_{p\mathrm{PLL}}s + K_{i\mathrm{PLL}}\right)} \quad (38)$$

where X^s_d and X^s_q represent the steady-state operating points, and $K_{p\mathrm{PLL}}$ and $K_{i\mathrm{PLL}}$ are the proportional and integral gains of the PI regulator of the PLL, respectively. V_{acd} represents the steady-state d-axis component of the PCC voltage. Hereafter, the superscript s represents the variables in the system-*dq* frame, while the superscript c denotes the variables in the *controller-dq* frame.

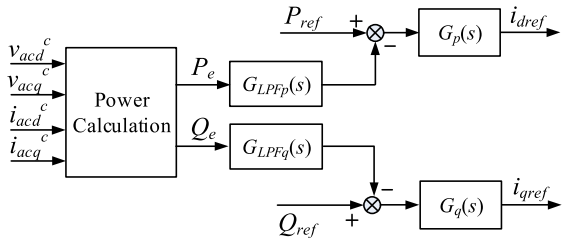

Fig. 6. Block diagram of the active and reactive power loops.

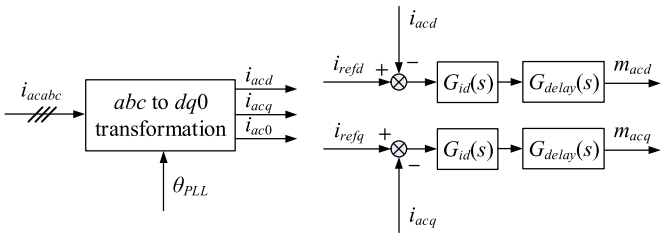

Fig. 7. Block diagram of the ac current control loop.

Fig. 6 shows the block diagram of the active/reactive power loop, where $G_{\mathrm{LPF}p}(s)$, $G_{\mathrm{LPF}q}(s)$ are the first-order low-pass filters (LPFs) used with the active/reactive power calculation and $G_p(s)$, $G_q(s)$ are the active/reactive power controllers. They are expressed as

$$G_{\mathrm{LPF}p}(s) = \frac{\omega_p}{s+\omega_p}, \quad G_{\mathrm{LPF}q}(s) = \frac{\omega_q}{s+\omega_q} \quad (39)$$

$$G_p(s) = K_{pp} + \frac{K_{pi}}{s}, \quad G_q(s) = K_{qp} + \frac{K_{qi}}{s} \quad (40)$$

where ω_p and ω_q are the crossover frequencies of $G_{\mathrm{LPF}p}(s)$ and $G_{\mathrm{LPF}q}(s)$, respectively. K_{pp}, K_{qp}, K_{pi}, K_{qi} are the proportional and integral gains for $G_p(s)$ and $G_q(s)$, respectively.

It should be noted that the ac current of the MMC does not have any zero-sequence components due to the three-phase–three-wire configuration [14], and thus the zero-sequence components do not need to be considered in the instantaneous active and reactive power calculation, which are given by [23]

$$\begin{aligned} P_e &= \frac{3}{2}\left(v^c_{\mathrm{acd}}i^c_{\mathrm{acd}} + v^c_{\mathrm{acq}}i^c_{\mathrm{acq}}\right) \\ Q_e &= \frac{3}{2}\left(v^c_{\mathrm{acd}}i^c_{\mathrm{acq}} - v^c_{\mathrm{acq}}i^c_{\mathrm{acd}}\right). \end{aligned} \quad (41)$$

The small-signal linearization of (41) can be expressed as

$$\begin{aligned} \hat{p}_e &= \frac{3}{2}\left(V_{\mathrm{acd}}\hat{i}^c_{\mathrm{acd}} + I_{\mathrm{acd}}\hat{v}^c_{\mathrm{acd}} + V_{\mathrm{acq}}\hat{i}^c_{\mathrm{acq}} + I_{\mathrm{acq}}\hat{v}^c_{\mathrm{acq}}\right) \\ \hat{q}_e &= \frac{3}{2}\left(V_{\mathrm{acd}}\hat{i}^c_{\mathrm{acq}} + I_{\mathrm{acq}}\hat{v}^c_{\mathrm{acd}} - V_{\mathrm{acq}}\hat{i}^c_{\mathrm{acd}} - I_{\mathrm{acd}}\hat{v}^c_{\mathrm{acq}}\right) \\ \Leftrightarrow \begin{bmatrix} \hat{p}_e \\ \hat{q}_e \end{bmatrix} &= \frac{3}{2}\left\{\begin{bmatrix} V_{\mathrm{acd}} & V_{\mathrm{acq}} \\ -V_{\mathrm{acq}} & V_{\mathrm{acd}} \end{bmatrix}\begin{bmatrix} \hat{i}^c_{\mathrm{acd}} \\ \hat{i}^c_{\mathrm{acq}} \end{bmatrix} + \begin{bmatrix} I_{\mathrm{acd}} & I_{\mathrm{acq}} \\ I_{\mathrm{acq}} & -I_{\mathrm{acd}} \end{bmatrix}\begin{bmatrix} \hat{v}^c_{\mathrm{acd}} \\ \hat{v}^c_{\mathrm{acq}} \end{bmatrix}\right\}. \end{aligned} \quad (42)$$

The dynamics of the active power loop and the reactive power loop can be expressed as

$$\begin{bmatrix}\hat{i}_{d\mathrm{ref}}\\ \hat{i}_{q\mathrm{ref}}\end{bmatrix} = -\begin{bmatrix} G_p(s)\,G_{\mathrm{LPF}p}(s) & \\ & G_q(s)\,G_{\mathrm{LPF}q}(s)\end{bmatrix}\begin{bmatrix}\hat{p}_e\\ \hat{q}_e\end{bmatrix} - \begin{bmatrix} G_{p1}(s) & \\ & G_{q1}(s)\end{bmatrix}\begin{bmatrix}\hat{p}_e\\ \hat{q}_e\end{bmatrix}. \tag{43}$$

Fig. 7 shows the block diagram of the ac current control loop. The PI controller is used as the ac current regulator, i.e., $G_{\mathrm{id}}(s) = K_{pid} + K_{iid}/s$, where K_{pid} and K_{iid} are the proportional and integral gains of the ac current regulator, respectively.

The dynamics of the ac current loop can be expressed as

$$\begin{aligned}\begin{bmatrix}\hat{m}^c_{\mathrm{acd}}\\ \hat{m}^c_{\mathrm{acq}}\end{bmatrix} &= \begin{bmatrix} G_{\mathrm{id}}(s)G_{\mathrm{delay}}(s) & \\ & G_{\mathrm{id}}(s)G_{\mathrm{delay}}(s)\end{bmatrix} \times \begin{bmatrix}\hat{i}_{\mathrm{ref}d} - \hat{i}^c_{\mathrm{acd}}\\ \hat{i}_{\mathrm{ref}q} - \hat{i}^c_{\mathrm{acq}}\end{bmatrix}\\ &\triangleq \begin{bmatrix} G_{\mathrm{id1}}(s) & \\ & G_{\mathrm{id1}}(s)\end{bmatrix}\begin{bmatrix}\hat{i}_{\mathrm{ref}d} - \hat{i}^c_{\mathrm{acd}}\\ \hat{i}_{\mathrm{ref}q} - \hat{i}^c_{\mathrm{acq}}\end{bmatrix}.\end{aligned} \tag{44}$$

Substituting (42) and (43) into (44) yields

$$\begin{aligned}\begin{bmatrix}\hat{m}^c_{\mathrm{acd}}\\ \hat{m}^c_{\mathrm{acq}}\end{bmatrix} &= -\frac{3}{2}\begin{bmatrix} I_{\mathrm{acd}}G_{\mathrm{id1}}G_{p1} & I_{\mathrm{acq}}G_{\mathrm{id1}}G_{p1}\\ I_{\mathrm{acq}}G_{\mathrm{id1}}G_{q1} & -I_{\mathrm{acd}}G_{\mathrm{id1}}G_{q1}\end{bmatrix}\begin{bmatrix}\hat{v}^c_{\mathrm{acd}}\\ \hat{v}^c_{\mathrm{acq}}\end{bmatrix}\\ &\quad - \left\{\frac{3}{2}\begin{bmatrix} V_{\mathrm{acd}}G_{\mathrm{id1}}G_{p1} & V_{\mathrm{acq}}G_{\mathrm{id1}}G_{p1}\\ -V_{\mathrm{acq}}G_{\mathrm{id1}}G_{q1} & V_{\mathrm{acd}}G_{\mathrm{id1}}G_{q1}\end{bmatrix} + \begin{bmatrix} G_{\mathrm{id1}} & \\ & G_{\mathrm{id1}}\end{bmatrix}\right\}\begin{bmatrix}\hat{i}^c_{\mathrm{acd}}\\ \hat{i}^c_{\mathrm{acq}}\end{bmatrix}.\end{aligned} \tag{45}$$

Consider $V_{\mathrm{acd}} = V_m$, $V_{\mathrm{acq}} = 0$ in the steady state, where V_m is the PCC voltage magnitude. Equation (45) can be simplified as

$$\begin{aligned}\begin{bmatrix}\hat{m}^c_{\mathrm{acd}}\\ \hat{m}^c_{\mathrm{acq}}\end{bmatrix} &= -\frac{3}{2}\begin{bmatrix} I_{\mathrm{acd}}G_{\mathrm{id1}}G_{p1} & I_{\mathrm{acq}}G_{\mathrm{id1}}G_{p1}\\ I_{\mathrm{acq}}G_{\mathrm{id1}}G_{q1} & -I_{\mathrm{acd}}G_{\mathrm{id1}}G_{q1}\end{bmatrix}\begin{bmatrix}\hat{v}^c_{\mathrm{acd}}\\ \hat{v}^c_{\mathrm{acq}}\end{bmatrix}\\ &\quad - \left\{\frac{3}{2}\begin{bmatrix} V_m G_{\mathrm{id1}}G_{p1} & \\ & V_m G_{\mathrm{id1}}G_{q1}\end{bmatrix} + \begin{bmatrix} G_{\mathrm{id1}} & \\ & G_{\mathrm{id1}}\end{bmatrix}\right\}\begin{bmatrix}\hat{i}^c_{\mathrm{acd}}\\ \hat{i}^c_{\mathrm{acq}}\end{bmatrix}.\end{aligned} \tag{46}$$

The corresponding complex-vector representation of (46) can be derived based on (18), which is given as (47) shown at the bottom of this page.

Equation (47) characterizes the dynamics of the active/reactive power loop and the ac current loop in the controller-dq frame. In order to include the dynamics of the PLL, (47) is further transformed into the system-dq frame based on (37), that is

$$\begin{aligned}\begin{bmatrix}\hat{m}^c_{\mathrm{acd}q+}\\ \hat{m}^c_{\mathrm{acd}q-}\end{bmatrix} &= \begin{bmatrix}\hat{m}^s_{\mathrm{acd}q+}\\ \hat{m}^s_{\mathrm{acd}q-}\end{bmatrix} - \frac{G_{\mathrm{PLL}}}{2}\begin{bmatrix} M_{\mathrm{acd}} + jM_{\mathrm{acq}} & -\left(M_{\mathrm{acd}} + jM_{\mathrm{acq}}\right)\\ -\left(M_{\mathrm{acd}} - jM_{\mathrm{acq}}\right) & M_{\mathrm{acd}} - jM_{\mathrm{acq}}\end{bmatrix} \times \begin{bmatrix}\hat{v}^s_{\mathrm{acd}q+}\\ \hat{v}^s_{\mathrm{acd}q-}\end{bmatrix}\end{aligned} \tag{48}$$

$$\begin{bmatrix}\hat{v}^c_{\mathrm{acd}q+}\\ \hat{v}^c_{\mathrm{acd}q-}\end{bmatrix} = \begin{bmatrix}\hat{v}^s_{\mathrm{acd}q+}\\ \hat{v}^s_{\mathrm{acd}q-}\end{bmatrix} - \frac{G_{\mathrm{PLL}}}{2}\begin{bmatrix} V_m & -V_m\\ -V_m & V_m\end{bmatrix}\begin{bmatrix}\hat{v}^s_{\mathrm{acd}q+}\\ \hat{v}^s_{\mathrm{acd}q-}\end{bmatrix} \tag{49}$$

$$\begin{aligned}\begin{bmatrix}\hat{i}^c_{\mathrm{acd}q+}\\ \hat{i}^c_{\mathrm{acd}q-}\end{bmatrix} &= \begin{bmatrix}\hat{i}^s_{\mathrm{acd}q+}\\ \hat{i}^s_{\mathrm{acd}q-}\end{bmatrix} - \frac{G_{\mathrm{PLL}}}{2}\begin{bmatrix} I_{\mathrm{acd}} + jI_{\mathrm{acq}} & -\left(I_{\mathrm{acd}} + jI_{\mathrm{acq}}\right)\\ -\left(I_{\mathrm{acd}} - jI_{\mathrm{acq}}\right) & I_{\mathrm{acd}} - jI_{\mathrm{acq}}\end{bmatrix}\begin{bmatrix}\hat{v}^s_{\mathrm{acd}q+}\\ \hat{v}^s_{\mathrm{acd}q-}\end{bmatrix}.\end{aligned} \tag{50}$$

Substituting (48)–(50) into (47) yields

$$\begin{bmatrix}\hat{m}^s_{\mathrm{acd}q+}\\ \hat{m}^s_{\mathrm{acd}q-}\end{bmatrix} = \mathbf{H_x}\begin{bmatrix}\hat{i}^s_{\mathrm{acd}q+}\\ \hat{i}^s_{\mathrm{acd}q-}\end{bmatrix} + \mathbf{H_v}\begin{bmatrix}\hat{v}^s_{\mathrm{acd}q+}\\ \hat{v}^s_{\mathrm{acd}q-}\end{bmatrix} \tag{51}$$

where $\mathbf{H_x}$ and $\mathbf{H_v}$ are given in Appendix C.

Equation (51) is further transformed to the system $\alpha\beta$ frame based on the dq–$\alpha\beta$ transformation [24], which yields

$$\begin{aligned}\begin{bmatrix}\hat{m}^s_{\mathrm{ac}\alpha\beta+}(s)\\ \hat{m}^s_{\mathrm{ac}\alpha\beta-}(s - 2j\omega_0)\end{bmatrix} &= \mathbf{H_x}\left(\mathbf{s} - \mathbf{j}\omega_\mathbf{0}\right)\begin{bmatrix}\hat{i}^s_{\mathrm{ac}\alpha\beta+}(s)\\ \hat{i}^s_{\mathrm{ac}\alpha\beta-}(s - 2j\omega_0)\end{bmatrix}\\ &\quad + \mathbf{H_v}\left(\mathbf{s} - \mathbf{j}\omega_\mathbf{0}\right)\begin{bmatrix}\hat{v}^s_{\mathrm{ac}\alpha\beta+}(s)\\ \hat{v}^s_{\mathrm{ac}\alpha\beta-}(s - 2j\omega_0)\end{bmatrix}.\end{aligned} \tag{52}$$

Substituting (33), (36), and (52) into (30), the closed-loop model of the MMC with/without the ZSCC control can be obtained.

$$\begin{aligned}\begin{bmatrix}\hat{m}^c_{\mathrm{acd}q+}\\ \hat{m}^c_{\mathrm{acd}q-}\end{bmatrix} &= -\frac{3}{2}\begin{bmatrix} \frac{I_{\mathrm{acd}}G_{\mathrm{id1}}(G_{p1} - G_{q1})}{2} + j\frac{I_{\mathrm{acq}}G_{\mathrm{id1}}(G_{q1} - G_{p1})}{2} & \frac{I_{\mathrm{acd}}G_{\mathrm{id1}}(G_{p1} + G_{q1})}{2} + j\frac{I_{\mathrm{acq}}G_{\mathrm{id1}}(G_{q1} + G_{p1})}{2}\\ \frac{I_{\mathrm{acd}}G_{\mathrm{id1}}(G_{p1} + G_{q1})}{2} - j\frac{I_{\mathrm{acq}}G_{\mathrm{id1}}(G_{q1} + G_{p1})}{2} & \frac{I_{\mathrm{acd}}G_{\mathrm{id1}}(G_{p1} - G_{q1})}{2} - j\frac{I_{\mathrm{acq}}G_{\mathrm{id1}}(G_{q1} - G_{p1})}{2}\end{bmatrix}\\ &\quad \times \begin{bmatrix}\hat{v}^c_{\mathrm{acd}q+}\\ \hat{v}^c_{\mathrm{acd}q-}\end{bmatrix} - \left\{\frac{3}{2}\begin{bmatrix} \frac{V_m G_{\mathrm{id1}}(G_{p1} + G_{q1})}{2} & \frac{V_m G_{\mathrm{id1}}(G_{p1} - G_{q1})}{2}\\ \frac{V_m G_{\mathrm{id1}}(G_{p1} - G_{q1})}{2} & \frac{V_m G_{\mathrm{id1}}(G_{p1} + G_{q1})}{2}\end{bmatrix} + \begin{bmatrix} G_{\mathrm{id1}} & \\ & G_{\mathrm{id1}}\end{bmatrix}\right\}\begin{bmatrix}\hat{i}^c_{\mathrm{acd}q+}\\ \hat{i}^c_{\mathrm{acd}q-}\end{bmatrix}\end{aligned} \tag{47}$$

TABLE I
MAIN CIRCUIT PARAMETERS OF THE MMC

SYMBOL	DESCRIPTION	VALUE
V_{grms}	RMS value of grid voltage (line to line)	100 kV
f_g	Grid frequency	50 Hz
P_o	Rated output power	100 MW
V_{dc}	DC side voltage	±100 kV
L_{arm}	Arm inductance	45 mH
R_{arm}	Arm resistance	0.15 Ω
C_{sm}	Capacitance of the submodule	3.3 mF
N	Number of the submodule each arm	100

IV. COMPLEX-VALUED IMPEDANCE MODELING AND ANALYSIS OF THE MMC WITH ZSCC CONTROL

In this section, a closed-loop SISO equivalent impedance model is derived for the grid-connected MMC, based on which the stability impact of the ZSCC control is analyzed. The main parameters of the MMC are given in Table I.

Rewriting (30) as

$$\begin{aligned}&\hat{\mathbf{x}}_{\boldsymbol{\alpha\beta}+-0}\\&=[\mathbf{sI}-(\mathbf{A}_{\mathbf{hss}\boldsymbol{\alpha\beta}+-\mathbf{0}}+\mathbf{B}_{\mathbf{mhss}\boldsymbol{\alpha\beta}+-\mathbf{0}}\mathbf{G}_{\mathbf{x}})]^{-1}\\&\quad\times(\mathbf{B}_{\mathbf{mhss}\boldsymbol{\alpha\beta}+-\mathbf{0}}\mathbf{G}_{\mathbf{v}}+\mathbf{B}_{\mathbf{vhss}\boldsymbol{\alpha\beta}+-\mathbf{0}})\hat{\mathbf{v}}_{\boldsymbol{\alpha\beta}+-0}=\mathbf{H}_{\mathbf{tfhss}}\hat{\mathbf{v}}_{\boldsymbol{\alpha\beta}+-0}\end{aligned} \tag{53}$$

Eq. (53) characterizes the relationships between the state variables $\hat{\mathbf{x}}_{\boldsymbol{\alpha\beta}+-0}$ and the disturbance input variables $\hat{\mathbf{v}}_{\boldsymbol{\alpha\beta}+-0}$. Due to the absence of the zero-sequence current path, the zero-sequence ac-side admittance of the three-phase–three-wire MMC system is zero. Yet, the admittance matrix from $\hat{v}_{\mathrm{ac}\alpha\beta+-}(s+jh\omega_0)$ to $\hat{i}_{\mathrm{ac}\alpha\beta+-}(s+jh\omega_0)$ is derived as the submatrix of the HTF matrix $\mathbf{H}_{\mathbf{tfhss}}$ in (53), which is given as (54) at the bottom of the next page, where the diagonal entries characterize the relationship between $\hat{i}_{\mathrm{ac}\alpha\beta+-}(s+jh\omega_0)$ and $\hat{v}_{\mathrm{ac}\alpha\beta+-}(s+jh\omega_0)$ at the same frequency, and the off-diagonal entries represent the frequency-coupling dynamics of the MMC.

The impedance matrix is the inverse of the admittance matrix, which is given as (55) at the bottom of the next page.

The recent studies in [13] and [25] have proven that the impedance model that includes the dc, fundamental frequency, and second-order-harmonic components of the steady-state operating trajectories is adequate for the stability analysis. Hence, (54) and (55) can be truncated as 10 × 10 matrices ($\mathbf{Y}_{\mathbf{MMC10}\times\mathbf{10}}$ and $\mathbf{Z}_{\mathbf{MMC10}\times\mathbf{10}}$).

Since the grid-connected MMC features frequency-coupling dynamics caused by its power stage, the active/reactive power control loop and the PLL, the off-diagonal elements in (54) and (55) are nonzero and their impacts on the system stability have to be accounted. In order to facilitate the stability analysis, instead of using the multivariable Nyquist criterion, a closed-loop SISO model of the MMC is developed, considering the frequency-coupling terms and the effect of the grid impedance.

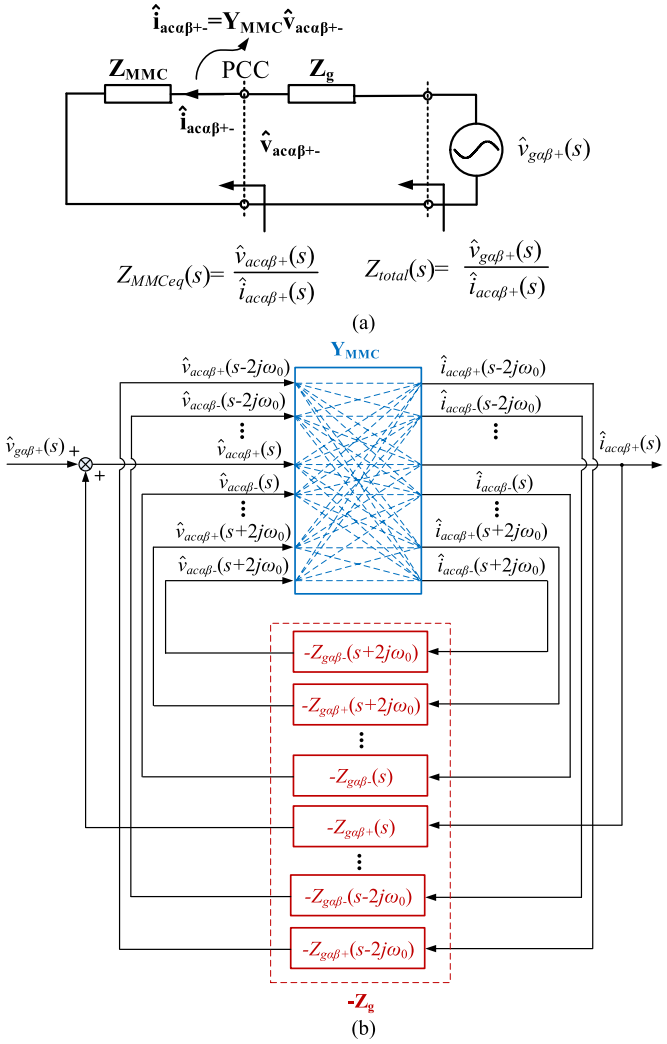

Fig. 8. Closed-loop representation of the MMC system. (a) Small-signal equivalent circuit. (b) Block diagram with cross-couplings.

Fig. 8(a) shows the small-signal equivalent circuit of the MMC system under the perturbation $\hat{v}_{g\alpha\beta+}(s)$. $\mathbf{Z_g}$ is the grid impedance matrix, which is diagonal for the three-phase balanced systems [24], and is given by

$$\mathbf{Z_g}=\mathrm{diag}[Z_{g\alpha\beta+}(s-2j\omega_0)\ldots Z_{g\alpha\beta+}(s)\ldots Z_{g\alpha\beta-}(s+2j\omega_0)]. \tag{56}$$

Fig. 8(b) shows the cross-couplings between different complex vectors of the impedance matrices in Fig. 8(a). The transfer function from $\hat{v}_{g\alpha\beta+}(s)$ to $\hat{i}_{\mathrm{ac}\alpha\beta+}(s)$, which represents the closed-loop SISO admittance of the system [19], [20], can be expressed as

$$\frac{\hat{i}_{\mathrm{ac}\alpha\beta+}(s)}{\hat{v}_{g\alpha\beta+}(s)}=Y_{\mathrm{total}}(s)=\mathbf{Y_{close}}(5,5) \tag{57}$$

where

$$\mathbf{Y_{close}}=\left(\mathbf{I}+\mathbf{Y_{MMC}}\mathbf{Z_g}\right)^{-1}\mathbf{Y_{MMC}}. \tag{58}$$

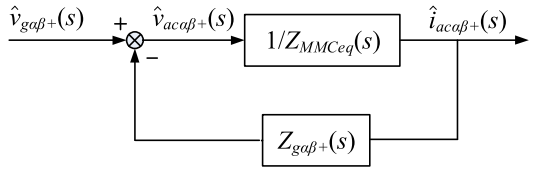

Fig. 9. SISO equivalent block diagram of the MMC system.

The relationship between $\hat{v}_{\mathrm{ac}\alpha\beta+}(s)$ and $\hat{i}_{\mathrm{ac}\alpha\beta+}(s)$ can also be derived based on Fig. 8(b), which is given by

$$\hat{v}_{\mathrm{ac}\alpha\beta+}(s) = \hat{v}_{g\alpha\beta+}(s) - \hat{i}_{\mathrm{ac}\alpha\beta+}(s)\, Z_{g\alpha\beta+}(s). \tag{59}$$

Defining the SISO equivalent ac impedance of the MMC as $Z_{\mathrm{MMCeq}}(s) = \hat{v}_{\mathrm{ac}\alpha\beta+}(s)/\hat{i}_{ac\alpha\beta+}(s)$ and dividing $\hat{i}_{\mathrm{ac}\alpha\beta+}(s)$ on both sides of (59) yields

$$Z_{\mathrm{MMCeq}}(s) = 1/Y_{\mathrm{total}}(s) - Z_{g\alpha\beta+}(s). \tag{60}$$

Based on (59) and (60), the SISO equivalent block diagram of Fig. 8(b) can be derived, as shown in Fig. 9. The system stability can then be assessed based on the loop gain $Z_{g\alpha\beta+}(s)/Z_{\mathrm{MMCeq}}(s)$. It is worth noting that $Z_{\mathrm{MMCeq}}(s)$ is calculated based on (57), (58), and (60), which includes the impact of frequency-coupling terms of the MMC and the grid impedance interaction, and is thus different from the centered-diagonal element $[Z_{0pp}(s)]$ in (55).

Fig. 10 shows the Bode diagrams of $Z_{0pp}(s)$ and $Z_{\mathrm{MMCeq}}(s)$ with and without the ZSCC control loop. The controller parameters are given in Table II, and the grid impedance is considered as 0.3-p.u. inductance. The impedance measurement results from the time-domain simulations are also given. It is clear that analytical results agree well with the simulation measurement, which confirms the correctness of the system modeling procedure given in Sections II and III. It is also observed that $Z_{0pp}(s)$ and $Z_{\mathrm{MMCeq}}(s)$ have different frequency responses both in magnitude and phase angles,

TABLE II
CONTROLLER PARAMETERS OF THE MMC

	Symbol	Value
Active Power Loop	K_{pp}	$8.2\cdot10^{-6}$/V
	K_{pi}	$1.3\cdot10^{-4}$/(V·s)
	ω_p	10π rad/s
Reactive Power Loop	K_{qp}	$8.2\cdot10^{-6}$/V
	K_{qi}	$2.6\cdot10^{-4}$/(V·s)
	ω_q	10π rad/s
PLL	K_{pPLL}	$2.6\cdot10^{-3}$ rad/(s·V)
	K_{iPLL}	0.29 rad/(s²·V)
AC Current Loop	K_{Pid}	$6.3\cdot10^{-4}\,\Omega$
	K_{iid}	0.32 Ω/s
Circulating Current Loop	K_{pic}	$9.4\cdot10^{-4}\,\Omega$
	K_{Ric}	$2.8\cdot10^{-3}\,\Omega$/s
	ω_{AD}	10π rad/s
Control Delay	T_d	200 μs

$$\hat{\mathbf{i}}_{\mathbf{ac}} = \mathbf{Y}_{\mathbf{MMC}}\hat{\mathbf{v}}_{\mathbf{ac}}$$

$$\mathbf{Y}_{\mathbf{MMC}} = \begin{bmatrix} \ddots & & \vdots & \vdots & & \iddots \\ & Y_{0pp}(s-j\omega_0) & Y_{0cpn}(s-j\omega_0) & Y_{-1pp}(s) & Y_{-1cpn}(s) & Y_{-2pp}(s+j\omega_0) & Y_{-2cpn}(s+j\omega_0) & \\ & Y_{0cnp}(s-j\omega_0) & Y_{0nn}(s-j\omega_0) & Y_{-1cnp}(s) & Y_{-1nn}(s) & Y_{-2cnp}(s+j\omega_0) & Y_{-2nn}(s+j\omega_0) & \\ \cdots & Y_{1pp}(s-j\omega_0) & Y_{1cpn}(s-j\omega_0) & Y_{0pp}(s) & Y_{0cpn}(s) & Y_{-1pp}(s+j\omega_0) & Y_{-1cpn}(s+j\omega_0) & \cdots \\ \cdots & Y_{1cnp}(s-j\omega_0) & Y_{1nn}(s-j\omega_0) & Y_{0cnp}(s) & Y_{0nn}(s) & Y_{-1cnp}(s+j\omega_0) & Y_{-1nn}(s+j\omega_0) & \cdots \\ & Y_{2pp}(s-j\omega_0) & Y_{2cpn}(s-j\omega_0) & Y_{1pp}(s) & Y_{1cpn}(s) & Y_{0pp}(s+j\omega_0) & Y_{0cpn}(s+j\omega_0) & \\ & Y_{2cnp}(s-j\omega_0) & Y_{2nn}(s-j\omega_0) & Y_{1cnp}(s) & Y_{1nn}(s) & Y_{0cnp}(s+j\omega_0) & Y_{0nn}(s+j\omega_0) & \\ \iddots & & \vdots & \vdots & & \ddots \end{bmatrix} \tag{54}$$

$$\hat{\mathbf{i}}_{\mathbf{ac}} = [\ldots\ \hat{i}_{\mathrm{ac}\alpha\beta+}(s-j\omega_0)\ \ \hat{i}_{\mathrm{ac}\alpha\beta-}(s-j\omega_0)\ \ \hat{i}_{\mathrm{ac}\alpha\beta+}(s)\ \ \hat{i}_{\mathrm{ac}\alpha\beta-}(s)\ \ \hat{i}_{\mathrm{ac}\alpha\beta+}(s+j\omega_0)\ \ \hat{i}_{\mathrm{ac}\alpha\beta-}(s+j\omega_0)\ \ \ldots]^T$$

$$\hat{\mathbf{v}}_{\mathbf{ac}} = [\ldots\ \hat{v}_{\mathrm{ac}\alpha\beta+}(s-j\omega_0)\ \ \hat{v}_{\mathrm{ac}\alpha\beta-}(s-j\omega_0)\ \ \hat{v}_{\mathrm{ac}\alpha\beta+}(s)\ \ \hat{v}_{\mathrm{ac}\alpha\beta-}(s)\ \ \hat{v}_{\mathrm{ac}\alpha\beta+}(s+j\omega_0)\ \ \hat{v}_{\mathrm{ac}\alpha\beta-}(s+j\omega_0)\ \ \ldots]^T$$

$$\mathbf{Z}_{\mathbf{MMC}} = \mathbf{Y}_{\mathbf{MMC}}^{-\mathbf{1}}$$

$$= \begin{bmatrix} \ddots & & \vdots & \vdots & & \iddots \\ & Z_{0pp}(s-j\omega_0) & Z_{0cpn}(s-j\omega_0) & Z_{-1pp}(s) & Z_{-1cpn}(s) & Z_{-2pp}(s+j\omega_0) & Z_{-2cpn}(s+j\omega_0) & \\ & Z_{0cnp}(s-j\omega_0) & Z_{0nn}(s-j\omega_0) & Z_{-1cnp}(s) & Z_{-1nn}(s) & Z_{-2cnp}(s+j\omega_0) & Z_{-2nn}(s+j\omega_0) & \\ \cdots & Z_{1pp}(s-j\omega_0) & Z_{1cpn}(s-j\omega_0) & Z_{0pp}(s) & Z_{0cpn}(s) & Z_{-1pp}(s+j\omega_0) & Z_{-1cpn}(s+j\omega_0) & \cdots \\ \cdots & Z_{1cnp}(s-j\omega_0) & Z_{1nn}(s-j\omega_0) & Z_{0cnp}(s) & Z_{0nn}(s) & Z_{-1cnp}(s+j\omega_0) & Z_{-1nn}(s+j\omega_0) & \cdots \\ & Z_{2pp}(s-j\omega_0) & Z_{2cpn}(s-j\omega_0) & Z_{1pp}(s) & Z_{1cpn}(s) & Z_{0pp}(s+j\omega_0) & Z_{0cpn}(s+j\omega_0) & \\ & Z_{2cnp}(s-j\omega_0) & Z_{2nn}(s-j\omega_0) & Z_{1cnp}(s) & Z_{1nn}(s) & Z_{0cnp}(s+j\omega_0) & Z_{0nn}(s+j\omega_0) & \\ \iddots & & \vdots & \vdots & & \ddots \end{bmatrix} \tag{55}$$

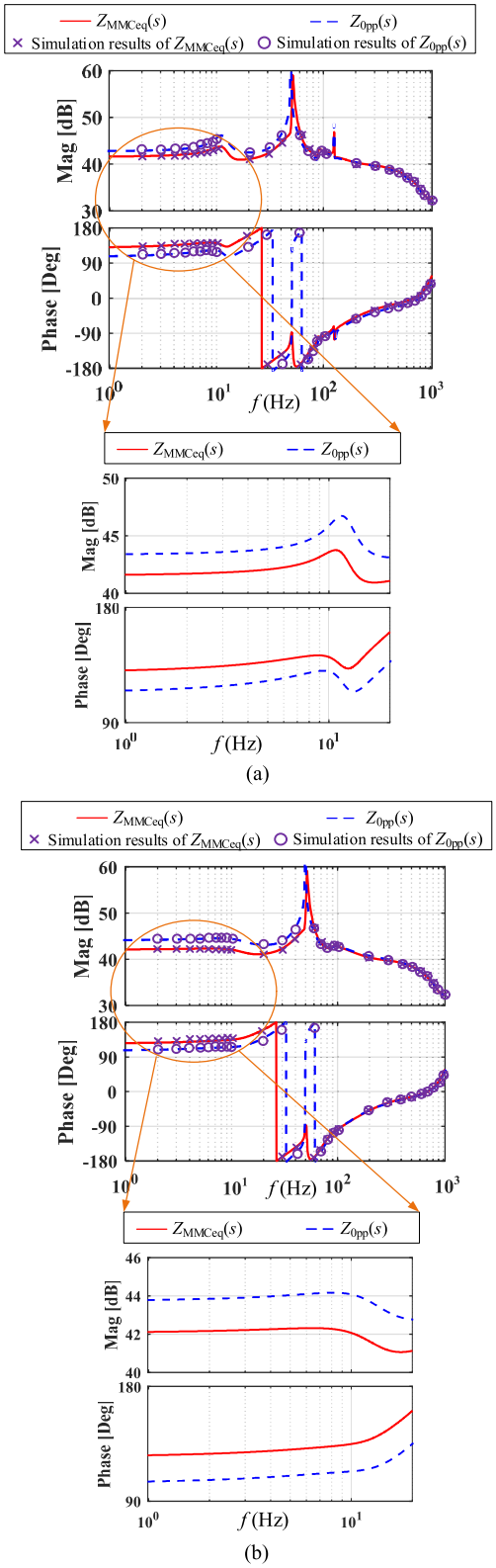

Fig. 10. Bode diagrams of $Z_{0pp}(s)$ and $Z_{\mathrm{MMCeq}}(s)$. (a) Without the ZSCC control. (b) With the ZSCC control ($R_{\mathrm{AD}} = 2 \times 10^{-2}$ p.u.).

especially in the low-frequency range (see the zoomed-in view of the figures), which implies that simply using $Z_{0pp}(s)$ for the stability analysis may lead to inaccurate predictions.

Fig. 11 shows the Bode diagrams of $Z_{\mathrm{MMCeq}}(s)$ with/without the ZSCC control and $Z_g(s)$. In this case, the grid impedance is considered as 0.5-p.u. inductance to represent a weak grid. It can be seen that the MMC without the ZSCC control introduces an additional resonant peak in $Z_{\mathrm{MMCeq}}(s)$. This resonant peak makes the phase difference at the magnitude intersection point of $Z_{\mathrm{MMCeq}}(s)$ and $Z_g(s)$ to be $189° > 180°$, as shown by the zoomed-in view in Fig. 11(a), which indicates the unstable operation of the system. In contrast, the resonant peak can be effectively damped by controlling the ZSCC, and the phase difference at the magnitude intersection point of Z_{MMCeq}(s) and $Z_g(s)$ is $168° < 180°$, as shown in Fig. 11(b), which indicates a stable operation of the system.

V. Parameter-Tuning Guideline for the ZSCC Control

A. Converter-Level Stability

Prior to analyzing the MMC-grid interactions, the stability of the MMC itself (i.e., with zero grid impedance) should be guaranteed first, which is defined as the converter-level stability hereafter. In order to solely investigate the stability impact of the ZSCC control loop, all other controller parameters are tuned based on the guideline provided in [26], which ensures that the MMC can operate stably without the ZSCC control, i.e., $R_{\mathrm{AD}} = 0$. As will be shown below, too large R_{AD} reduces the phase margin (PM) of the ZSCC control loop and may jeopardize the converter-level stability of the MMC, and thus, the critical value of R_{AD}, which leads to PM $= 0$, will be derived as follows.

The crossover frequency (f_c) of the current loop of the MMC is usually tuned around 1/20∼1/10 of its control frequency. A typical control frequency of the MMC is 10 kHz [27], which leads to $f_c = 500 \sim 1000$ Hz. It has been found in [13] and [25] that the dynamic impact of the capacitor voltage ripple of the MMC is negligible in this frequency range, and thus, $v_{c\Sigma} = 2V_{\mathrm{dc}}$ and $v_{c\Delta} = 0$ can be assumed when calculating the PM of the ZSCC control loop at f_c. Consequently, (5) can be simplified as

$$v_{\mathrm{dc}} - m_{\mathrm{dc}i} V_{\mathrm{dc}} = 2L_{\mathrm{arm}} \frac{di_{ciri}}{dt} + 2R_{\mathrm{arm}} i_{ciri}. \tag{61}$$

The dynamics of the ZSCC can be characterized by summing up three phase quantities in (61), which yields

$$\begin{aligned} &\frac{1}{3} \sum_{i=a.b.c} (v_{\mathrm{dc}} - m_{\mathrm{dc}i} V_{\mathrm{dc}}) \\ &\quad = \frac{1}{3} \sum_{i=a.b.c} \left(2L_{\mathrm{arm}} \frac{di_{ciri}}{dt} + 2R_{\mathrm{arm}} i_{ciri} \right) \\ &\quad \Leftrightarrow v_{\mathrm{dc}} - m_{\mathrm{dc}0} V_{\mathrm{dc}} = 2L_{\mathrm{arm}} \frac{di_{cir0}}{dt} + 2R_{\mathrm{arm}} i_{cir0} \end{aligned} \tag{62}$$

where $m_{\mathrm{dc}0}$ is determined by the ZSCC control given in (35).

Substituting (35) into (62) and transforming the result into s domain yields

$$\begin{aligned} &v_{\mathrm{dc}}(s) - V_{\mathrm{dc}} G_{\mathrm{AD}}(s)\, G_{\mathrm{delay}}(s)\, i_{cir0}(s) \\ &\quad = 2(sL_{\mathrm{arm}} + R_{\mathrm{arm}})\, i_{cir0}(s) \end{aligned} \tag{63}$$

$$G_{\mathrm{AD}}(s) = R_{\mathrm{AD}} \frac{s}{s + \omega_{\mathrm{AD}}}, \quad G_{\mathrm{delay}}(s) = e^{-sT_d} \tag{64}$$

where T_d is the control delay of the MMC.

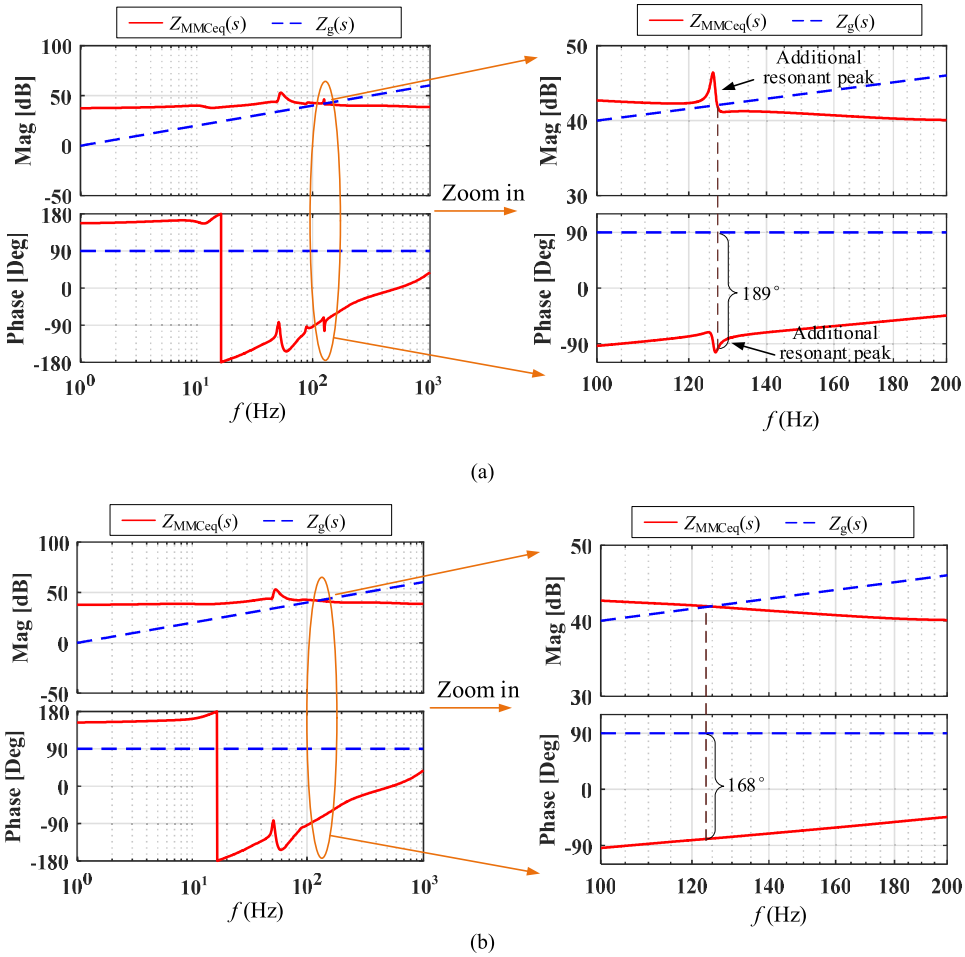

Fig. 11. Bode diagram of $Z_{\mathrm{MMCeq}}(s)$ and $Z_g(s)$. (a) Without the ZSCC control. (b) With the ZSCC control ($R_{\mathrm{AD}} = 2 \times 10^{-2}$ p.u.).

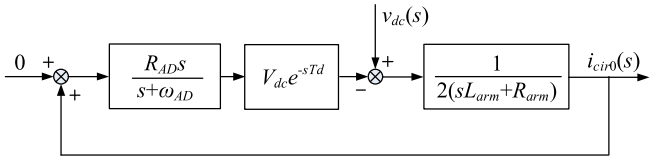

Fig. 12. Block diagram of the ZSCC control loop.

Based on (63) and (64), the block diagram of the ZSCC control loop can be plotted, as shown in Fig. 12, and the loop gain can be derived as

$$T_{\mathrm{ZSCC}}(s) = \frac{V_{\mathrm{dc}} R_{\mathrm{AD}} e^{-sT_d}}{2(sL_{\mathrm{arm}} + R_{\mathrm{arm}})} \frac{s}{s + \omega_{\mathrm{AD}}}. \tag{65}$$

It is noted that ω_{AD} is usually selected around several hertz in order to guarantee the effective active damping in a wide frequency range, and thus, $s/(s + \omega_{\mathrm{AD}})$ can be approximated as the unity gain at f_c. Moreover, since the arm resistance is much smaller than the arm inductance at f_c, the magnitude of the loop gain at f_c can be approximated as

$$|T_{\mathrm{ZSCC}}(j2\pi f_c)| \approx \frac{V_{\mathrm{dc}} R_{\mathrm{AD}}}{2 \cdot 2\pi f_c L_{\mathrm{arm}}} = 1 \tag{66}$$

and the corresponding PM can be calculated as

$$\mathrm{PM} = \frac{\pi}{2} - 2\pi f_c T_d. \tag{67}$$

It is known from (66) and (67) that larger R_{AD} leads to the increased f_c, but the decreased PM. The upper limit of the R_{AD} can be calculated by substituting PM = 0 into (66) and (67), which yields

$$R_{\mathrm{AD\,max}} = \frac{\pi L_{\mathrm{arm}}}{V_{\mathrm{dc}} T_d}. \tag{68}$$

Based on the parameters in Tables I and II, it can be calculated that $R_{\mathrm{ADmax}} = 0.65$ p.u. in this article.

B. System-Level Stability

By selecting $R_{\mathrm{AD}} < R_{\mathrm{ADmax}}$, the converter-level stability of the MMC can be guaranteed. Then, the stability of the MMC under the weak grid condition, which is defined as the system-level stability hereafter, requires that $Z_g(s)/Z_{\mathrm{MMCeq}}(s)$ satisfies the Nyquist stability criterion. Fig. 13 shows the zoomed-in view of the Bode diagram of $Z_g(s)$ and $Z_{\mathrm{MMCeq}}(s)$ with different values of R_{AD}, and it is clear that too small R_{AD} cannot provide sufficient damping on the resonant peak, leading to a phase difference at the magnitude intersection point of $Z_{\mathrm{MMCeq}}(s)$ and $Z_g(s)$ above 180°, as shown in

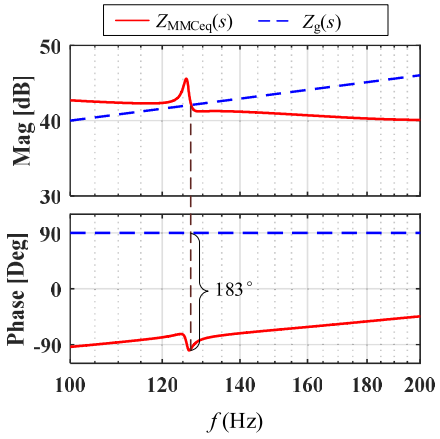

(a)

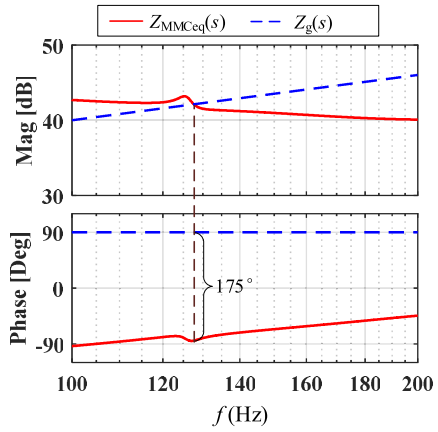

(b)

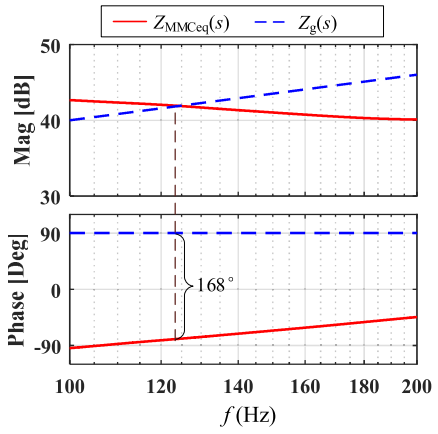

(c)

Fig. 13. Zoomed-in view of the Bode diagram of $Z_{\mathrm{MMCeq}}(s)$ and $Z_g(s)$ with the ZSCC control. (a) $R_{\mathrm{AD}} = 2 \times 10^{-4}$ p.u. (b) $R_{\mathrm{AD}} = 2 \times 10^{-3}$ p.u. (c) $R_{\mathrm{AD}} = 2 \times 10^{-2}$ p.u.

Fig. 13(a), which implies an unstable operation of the system. The analytical solution for the lower limit of R_{AD} is challenging due to the complicated expression of $Z_{\mathrm{MMCeq}}(s)$. Therefore, R_{ADmin} is calculated numerically based on an iterative procedure shown in Fig. 14. R_{AD} is initialized with zero and then increased with a fixed step size during every

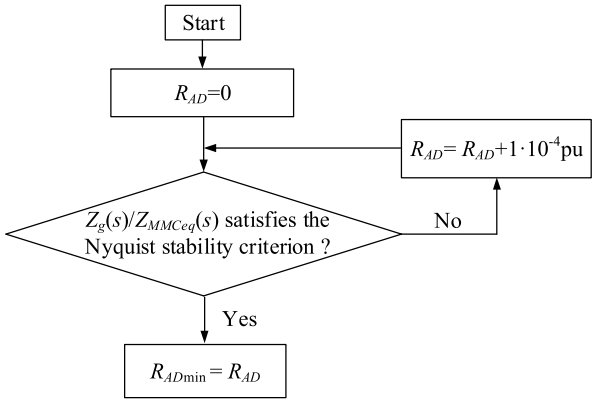

Fig. 14. Iterative procedure for calculating R_{ADmin}.

iteration until the stability criterion is met. Based on the parameters given in Tables I and II, it can be calculated that $R_{\mathrm{ADmin}} = 1.3 \times 10^{-3}$ p.u. Therefore, R_{AD} should be selected in the range between R_{ADmin} and R_{ADmax} to guarantee the stability of the MMC.

It is worth noting that the calculation of R_{ADmin} requires the prior knowledge of the grid impedance. In practice, the value of the grid impedance at the PCC maybe time-varying due to the change in the grid configurations and/or the load conditions. Therefore, the selection of R_{ADmin} should consider the worst case where the grid impedance reaches its maximum value ($Z_{g\mathrm{max}}$), which can be calculated based on the relationship $|Z_{g\mathrm{max}}|$ (p.u.) = $1/\mathrm{SCR}_{\mathrm{min}}$ [28], where $\mathrm{SCR}_{\mathrm{min}}$ is the minimum short-circuit ratio (SCR) at the PCC, and this value can be obtained from the power system operator [29].

VI. Simulation Verification

To validate the theoretical analysis, time-domain simulations are carried out in the MATLAB/Simulink and PLECS blockset. The parameters given in Tables I and II are adopted in simulations. Two operating scenarios that consider both the stiff grid ($Z_g(s) = 0$) and the weak grid ($Z_g(s) = 0.5$ p.u.) are evaluated in simulations.

Fig. 15 shows the simulation results of the MMC connected to the stiff grid ($Z_g(s) = 0$). In this case, the MMC can work stably without the ZSCC control or with the ZSCC control and $R_{\mathrm{AD}} < R_{\mathrm{Admax}}$, as shown in Fig. 15(a)–(c). The second-order-harmonic circulating current is around 2.4% of its dc value in these cases, indicating that this second-order-harmonic circulating current is effectively suppressed by the CCSC. However, if $R_{\mathrm{AD}} > R_{\mathrm{ADmax}}$, the high-frequency oscillation appears in the ac current and the circulating current, as shown in Fig. 15(d), which indicates the unstable operation of the system. The Fourier analysis results show that the oscillation frequency in the circulating current is 1.24 kHz, which approximates the theoretical calculated value based on (67), i.e., 1.25 kHz. The simulation results verify the theoretical analysis presented in Section V-A.

Fig. 16 shows the simulation results of the MMC connected to the weak grid [$Z_g(s) = 0.5$ p.u.]. It can be seen that the MMC becomes unstable without the ZSCC control and with

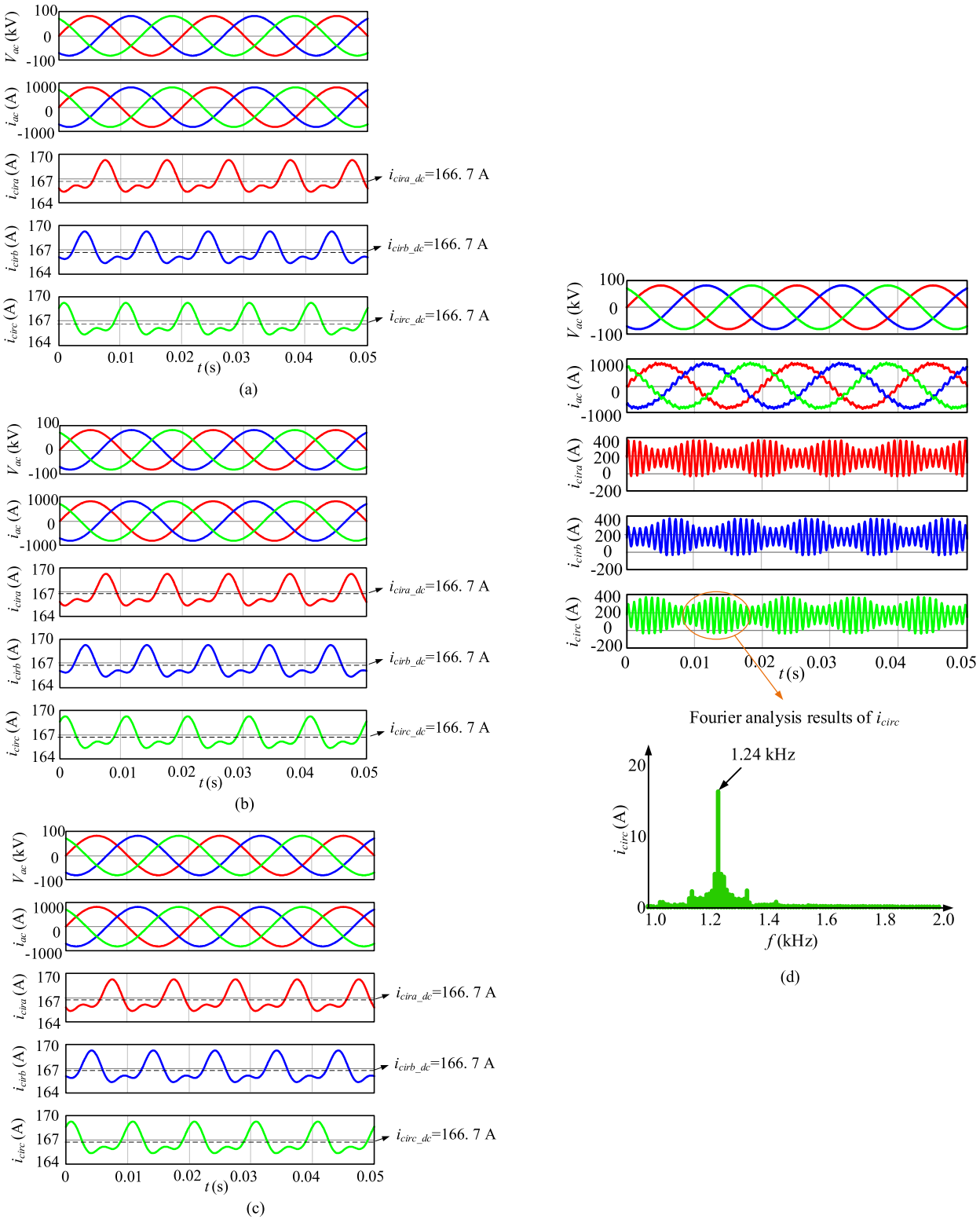

Fig. 15. Time-domain simulation results of the MMC connecting to the strong ac grid [$Z_g(s) = 0$]. (a) Without the ZSCC control, stable. (b) With the ZSCC control and $R_{\mathrm{AD}} = 2 \times 10^{-4}$ p.u. $< R_{\mathrm{ADmax}}$, stable. (c) With the ZSCC control and $R_{\mathrm{AD}} = 2 \times 10^{-2}$ p.u. $< R_{\mathrm{ADmax}}$, stable. (d) With the ZSCC control and $R_{\mathrm{AD}} = 6.7 \times 10^{-1}$ p.u. $> R_{\mathrm{ADmax}}$, unstable.

the ZSCC control but $R_{\mathrm{AD}} < R_{\mathrm{ADmin}}$, and the oscillation appears in the ac output voltage/current of the MMC, as shown in Fig. 16(a) and (b), which agree with the stability analysis given in Figs. 11(a) and 13(a). Moreover, due to the coupling between the ac-side dynamics and internal dynamics of the MMC, the ac-side voltage/current oscillations further lead to the ZSCC oscillation, as confirmed by the simulation results shown in Fig. 16(a) and (b). In contrast, the system can work

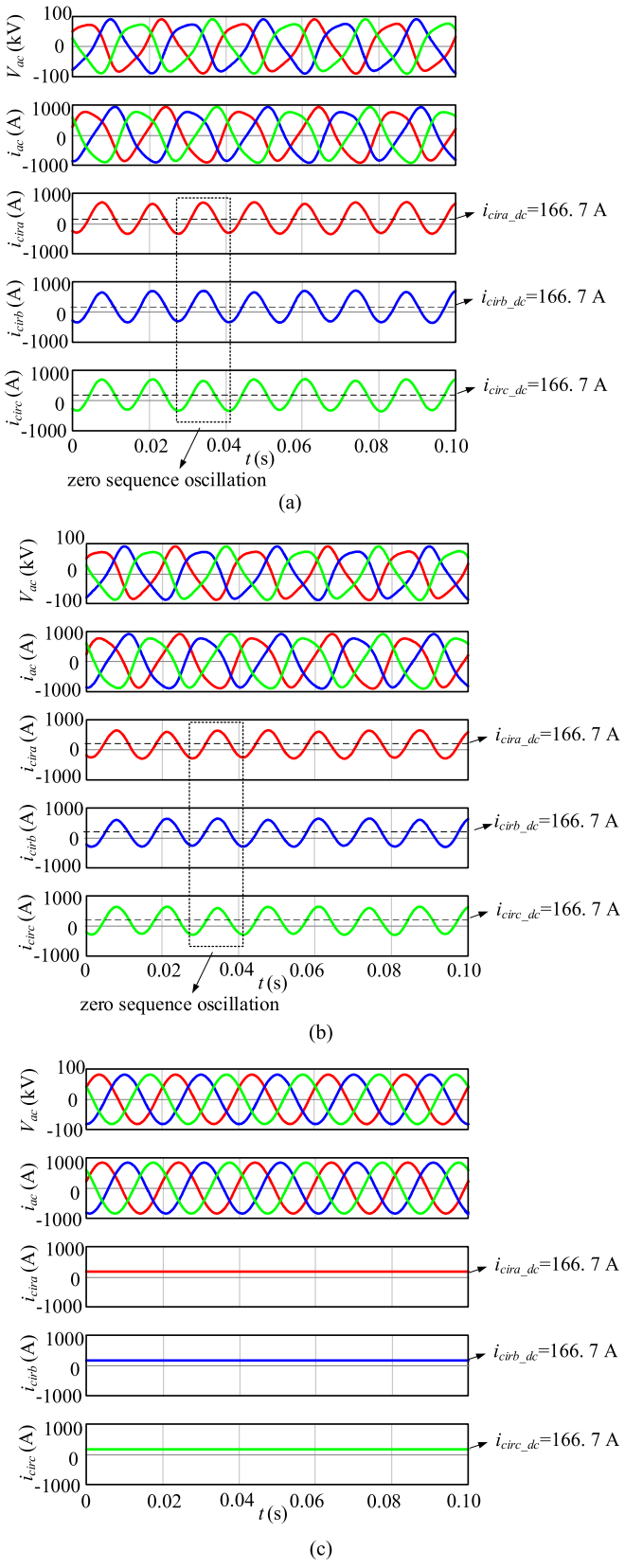

Fig. 16. Time-domain simulation results of the MMC connecting to the weak ac grid [$Z_g(s) = 0.5$ p.u.]. (a) Without the ZSCC control, unstable (b) With the ZSCC control and $R_{\mathrm{AD}} = 2 \times 10^{-4}$ p.u. $< R_{\mathrm{ADmin}}$, unstable (c) With the ZSCC control and $R_{\mathrm{AD}} = 2 \times 10^{-2}$ p.u. $> R_{\mathrm{ADmin}}$, stable.

stably if the ZSCC is under control and $R_{\mathrm{AD}} > R_{\mathrm{ADmin}}$, as shown in Fig. 16(c), which confirms the theoretical analysis given in Fig. 13(c).

VII. Conclusion

In this article, the ac-side impedance model that is based on complex vectors and HTFs has been developed for the grid-connected MMC. Based on the model, an SISO closed-loop total admittance of the MMC-grid system that includes the effect of the frequency coupling dynamics of the MMC and the grid impedance has been formulated, from which an equivalent SISO ac impedance of the MMC has been further derived. With this SISO representation, the impacts of the ZSCC control on the ac-side dynamics of the MMC have been explicitly revealed. The frequency-domain analysis and time-domain simulations have shown the resonant peaks in the equivalent SISO ac impedance of the MMC due to the absence of the ZSCC control, which tends to destabilize the system when interacting with the grid impedance. To guarantee the system stability, a systematic parameter-tuning guideline for the ZSCC control loop has also been developed, and its effectiveness has been confirmed by case studies in simulations. The findings of this article complement the dc-side dynamic analysis in previous works, highlighting the necessity of utilizing the ZSCC control to stabilize both the dc- and ac-side dynamics of the MMC even in three-phase balanced power systems.

Appendix A

$\mathbf{A_{abc}(t)}$ and $\mathbf{B_{abc}(t)}$ in (15) are given by (A.1) and (A.2), as shown at the bottom of the next page.

Appendix B

A general LTP system can be expressed as

$$\begin{aligned} \frac{d\hat{x}(t)}{dt} &= A(t)\hat{x}(t) + B(t)\hat{u}(t) \\ \hat{y}(t) &= C(t)\hat{x}(t) + D(t)\hat{u}(t) \end{aligned} \tag{B.1}$$

where $\hat{x}(t)$, $\hat{u}(t)$, and $\hat{y}(t)$ are the state variables, input variables, and output variables, respectively. $A(t)$, $B(t)$, $C(t)$, and $D(t)$ are the time-periodic matrices, which can be expressed as Fourier series, that is

$$\begin{aligned} A(t) &= \sum_{h=-\infty}^{+\infty} A_h e^{jh\omega_0 t} \\ B(t) &= \sum_{h=-\infty}^{+\infty} B_h e^{jh\omega_0 t} \\ C(t) &= \sum_{h=-\infty}^{+\infty} C_h e^{jh\omega_0 t} \\ D(t) &= \sum_{h=-\infty}^{+\infty} D_h e^{jh\omega_0 t} \end{aligned} \tag{B.2}$$

where A_h, B_h, C_h, and D_h are the corresponding hth Fourier coefficients of $A(t)$, $B(t)$, $C(t)$, and $D(t)$, respectively.

Substituting (B.2) into (B.1) and transforming (B.1) into the s-domain, the HSS model of (B.1) can be directly obtained, which are expressed as [22]

$$\begin{aligned} s\hat{\mathbf{x}} &= \mathbf{A_{hss}}\hat{\mathbf{x}} + \mathbf{B_{hss}}\hat{\mathbf{u}} \\ \hat{\mathbf{y}} &= \mathbf{C_{hss}}\hat{\mathbf{x}} + \mathbf{D_{hss}}\hat{\mathbf{u}} \end{aligned} \tag{B.3}$$

where

$$\begin{aligned} \hat{\mathbf{x}} &= [\cdots \hat{X}_{-h} \cdots \hat{X}_{-1}\ \hat{X}_0\ \hat{X}_1 \cdots \hat{X}_h \cdots]^T \\ \hat{\mathbf{u}} &= [\cdots \hat{U}_{-h} \cdots \hat{U}_{-1}\ \hat{U}_0\ \hat{U}_1 \cdots \hat{U}_h \cdots]^T \\ \hat{\mathbf{y}} &= [\cdots \hat{Y}_{-h} \cdots \hat{Y}_{-1}\ \hat{Y}_0\ \hat{Y}_1 \cdots \hat{Y}_h \cdots]^T \end{aligned} \tag{B.4}$$

$$\begin{aligned} \mathbf{A_{hss}} &= \Gamma[A] - \mathbf{N} \\ \mathbf{B_{hss}} &= \Gamma[B] \\ \mathbf{C_{hss}} &= \Gamma[C] \\ \mathbf{D_{hss}} &= \Gamma[D]. \end{aligned} \tag{B.5}$$

$\mathbf{N}$ is the diagonal matrix, which is expressed as

$$\mathbf{N} = \text{diag}[-jh\omega_0\mathbf{I} \ \cdots \ -j\omega_0\mathbf{I}\ \ \mathbf{I}\ \ j\omega_0\mathbf{I} \ \cdots \ jh\omega_0\mathbf{I}] \tag{B.6}$$

where $\mathbf{I}$ is the identity matrix, $\mathbf{\Gamma}$ represents the Toeplitz matrix, and $\mathbf{\Gamma}[A]$ is expressed as

$$\Gamma[A] = \begin{bmatrix} \cdots & \cdots & \cdots & \cdots & \cdots & \cdots \\ \cdots & A_0 & A_{-1} & \cdots & A_{-h} & \cdots \\ \cdots & A_1 & A_0 & \cdots & A_{-h+1} & \cdots \\ \cdots & \cdots & \cdots & \cdots & \cdots & \cdots \\ \cdots & A_h & A_{h-1} & \cdots & A_0 & \cdots \\ \cdots & \cdots & \cdots & \cdots & \cdots & \cdots \end{bmatrix}. \tag{B.7}$$

$\mathbf{\Gamma}[B]$, $\mathbf{\Gamma}[C]$, and $\mathbf{\Gamma}[D]$ have similar expressions, and thus are not reproduced here. It is noted that the elements of the matrices $\mathbf{A_{hss}}$, $\mathbf{B_{hss}}$, $\mathbf{C_{hss}}$, and $\mathbf{D_{hss}}$ are the Fourier coefficients of $A(t)$, $B(t)$, $C(t)$, and $D(t)$, which are constant values. Therefore, the HSS model essentially derives the LTI representation of the LTP system, and thus, the linear control theory can be readily used. Moreover, although the HSS model can include the infinite number of harmonic components in theory, only the major harmonic components of the system are considered in the practical modeling procedure [22].

$\mathbf{A_{abc}(t)}$

$$= \begin{bmatrix} -\frac{R_{\text{arm}}}{L_{\text{arm}}} & 0 & 0 & 0 & 0 & 0 & \frac{2M_{aca}(t)}{3L_{\text{arm}}} & -\frac{M_{acb}(t)}{3L_{\text{arm}}} & -\frac{M_{acc}(t)}{3L_{\text{arm}}} & -\frac{M_{dca}(t)}{3L_{\text{arm}}} & \frac{M_{dcb}(t)}{6L_{\text{arm}}} & \frac{M_{dcc}(t)}{6L_{\text{arm}}} \\ 0 & -\frac{R_{\text{arm}}}{L_{\text{arm}}} & 0 & 0 & 0 & 0 & -\frac{M_{aca}(t)}{3L_{\text{arm}}} & \frac{2M_{acb}(t)}{3L_{\text{arm}}} & -\frac{M_{acc}(t)}{3L_{\text{arm}}} & \frac{M_{dca}(t)}{6L_{\text{arm}}} & -\frac{M_{dcb}(t)}{3L_{\text{arm}}} & \frac{M_{dcc}(t)}{6L_{\text{arm}}} \\ 0 & 0 & -\frac{R_{\text{arm}}}{L_{\text{arm}}} & 0 & 0 & 0 & -\frac{M_{aca}(t)}{3L_{\text{arm}}} & -\frac{M_{acb}(t)}{3L_{\text{arm}}} & \frac{2M_{acc}(t)}{3L_{\text{arm}}} & \frac{M_{dca}(t)}{6L_{\text{arm}}} & \frac{M_{dcb}(t)}{6L_{\text{arm}}} & -\frac{M_{dcc}(t)}{3L_{\text{arm}}} \\ 0 & 0 & 0 & -\frac{R_{\text{arm}}}{L_{\text{arm}}} & 0 & 0 & -\frac{M_{dca}(t)}{4L_{\text{arm}}} & 0 & 0 & \frac{M_{aca}(t)}{2L_{\text{arm}}} & 0 & 0 \\ 0 & 0 & 0 & 0 & -\frac{R_{\text{arm}}}{L_{\text{arm}}} & 0 & 0 & -\frac{M_{dcb}(t)}{4L_{\text{arm}}} & 0 & 0 & \frac{M_{acb}(t)}{2L_{\text{arm}}} & 0 \\ 0 & 0 & 0 & 0 & 0 & -\frac{R_{\text{arm}}}{L_{\text{arm}}} & 0 & 0 & -\frac{M_{dcc}(t)}{4L_{\text{arm}}} & 0 & 0 & \frac{M_{acc}(t)}{2L_{\text{arm}}} \\ -\frac{NM_{aca}(t)}{C} & 0 & 0 & \frac{NM_{dca}(t)}{C} & 0 & 0 & 0 & 0 & 0 & 0 & 0 & 0 \\ 0 & -\frac{NM_{acb}(t)}{C} & 0 & 0 & \frac{NM_{dcb}(t)}{C} & 0 & 0 & 0 & 0 & 0 & 0 & 0 \\ 0 & 0 & -\frac{NM_{acc}(t)}{C} & 0 & 0 & \frac{NM_{dcc}(t)}{C} & 0 & 0 & 0 & 0 & 0 & 0 \\ \frac{NM_{dca}(t)}{2C} & 0 & 0 & -\frac{2NM_{aca}(t)}{C} & 0 & 0 & 0 & 0 & 0 & 0 & 0 & 0 \\ 0 & \frac{NM_{dcb}(t)}{2C} & 0 & 0 & -\frac{2NM_{acb}(t)}{C} & 0 & 0 & 0 & 0 & 0 & 0 & 0 \\ 0 & 0 & \frac{NM_{dcc}(t)}{2C} & 0 & 0 & -\frac{2NM_{acc}(t)}{C} & 0 & 0 & 0 & 0 & 0 & 0 \end{bmatrix} \tag{A.1}$$

$\mathbf{B_{abc}(t)}$

$$= \begin{bmatrix} \frac{2V_c\sum a(t)}{3L_{\text{arm}}} & -\frac{V_c\sum b(t)}{3L_{\text{arm}}} & -\frac{V_c\sum c(t)}{3L_{\text{arm}}} & -\frac{V_{c\Delta a}(t)}{3L_{\text{arm}}} & \frac{V_{c\Delta b}(t)}{6L_{\text{arm}}} & \frac{V_{c\Delta c}(t)}{6L_{\text{arm}}} & -\frac{2}{L_{\text{arm}}} & 0 & 0 & 0 & 0 & 0 \\ -\frac{V_c\sum a(t)}{3L_{\text{arm}}} & \frac{2V_c\sum b(t)}{3L_{\text{arm}}} & -\frac{V_c\sum c(t)}{3L_{\text{arm}}} & \frac{V_{c\Delta a}(t)}{6L_{\text{arm}}} & -\frac{V_{c\Delta b}(t)}{3L_{\text{arm}}} & \frac{V_{c\Delta c}(t)}{6L_{\text{arm}}} & 0 & -\frac{2}{L_{\text{arm}}} & 0 & 0 & 0 & 0 \\ -\frac{V_c\sum a(t)}{3L_{\text{arm}}} & -\frac{V_c\sum b(t)}{3L_{\text{arm}}} & \frac{2V_c\sum c(t)}{3L_{\text{arm}}} & \frac{V_{c\Delta a}(t)}{6L_{\text{arm}}} & \frac{V_{c\Delta b}(t)}{6L_{\text{arm}}} & -\frac{V_{c\Delta c}(t)}{3L_{\text{arm}}} & 0 & 0 & -\frac{2}{L_{\text{arm}}} & 0 & 0 & 0 \\ \frac{V_{c\Delta a}(t)}{2L_{\text{arm}}} & 0 & 0 & -\frac{V_c\sum a(t)}{4L_{\text{arm}}} & 0 & 0 & 0 & 0 & 0 & \frac{1}{2L_{\text{arm}}} & 0 & 0 \\ 0 & \frac{V_{c\Delta b}(t)}{2L_{\text{arm}}} & 0 & 0 & -\frac{V_c\sum b(t)}{4L_{\text{arm}}} & 0 & 0 & 0 & 0 & 0 & \frac{1}{2L_{\text{arm}}} & 0 \\ 0 & 0 & \frac{V_{c\Delta c}(t)}{2L_{\text{arm}}} & 0 & 0 & -\frac{V_c\sum c(t)}{4L_{\text{arm}}} & 0 & 0 & 0 & 0 & 0 & \frac{1}{2L_{\text{arm}}} \\ -\frac{N}{C}I_{aca}(t) & 0 & 0 & \frac{N}{C}I_{cira}(t) & 0 & 0 & 0 & 0 & 0 & 0 & 0 & 0 \\ 0 & -\frac{N}{C}I_{acb}(t) & 0 & 0 & \frac{N}{C}I_{cirb}(t) & 0 & 0 & 0 & 0 & 0 & 0 & 0 \\ 0 & 0 & -\frac{N}{C}I_{acc}(t) & 0 & 0 & \frac{N}{C}I_{circ}(t) & 0 & 0 & 0 & 0 & 0 & 0 \\ -\frac{2N}{C}I_{cira}(t) & 0 & 0 & \frac{N}{2C}I_{aca}(t) & 0 & 0 & 0 & 0 & 0 & 0 & 0 & 0 \\ 0 & -\frac{2N}{C}I_{cirb}(t) & 0 & 0 & \frac{N}{2C}I_{acb}(t) & 0 & 0 & 0 & 0 & 0 & 0 & 0 \\ 0 & 0 & -\frac{2N}{C}I_{cic}(t) & 0 & 0 & \frac{N}{2C}I_{acc}(t) & 0 & 0 & 0 & 0 & 0 & 0 \end{bmatrix} \tag{A.2}$$

$$\mathbf{H_x} = -\frac{3}{2}\begin{bmatrix} \frac{V_m G_{\mathrm{id1}}(G_{p1}+G_{q1})}{2} & \frac{V_m G_{\mathrm{id1}}(G_{p1}-G_{q1})}{2} \\ \frac{V_m G_{\mathrm{id1}}(G_{p1}-G_{q1})}{2} & \frac{V_m G_{\mathrm{id1}}(G_{p1}+G_{q1})}{2} \end{bmatrix} - \begin{bmatrix} G_{\mathrm{id1}} & \\ & G_{\mathrm{id1}} \end{bmatrix} \tag{C.1}$$

$$\begin{aligned} \mathbf{H_v} = {} & \frac{G_{\mathrm{PLL}}}{2}\begin{bmatrix} M_{\mathrm{acd}}+jM_{\mathrm{acq}} & -(M_{\mathrm{acd}}+jM_{\mathrm{acq}}) \\ -(M_{\mathrm{acd}}-jM_{\mathrm{acq}}) & M_{\mathrm{acd}}-jM_{\mathrm{acq}} \end{bmatrix} + \frac{3}{2}\left(\frac{G_{\mathrm{PLL}}}{2}V_m - 1\right) \\ & \times \begin{bmatrix} \frac{I_{\mathrm{acd}}G_{\mathrm{id1}}(G_{p1}-G_{q1})}{2} + j\frac{I_{\mathrm{acq}}G_{\mathrm{id1}}(G_{q1}-G_{p1})}{2} & \frac{I_{\mathrm{acd}}G_{\mathrm{id1}}(G_{p1}+G_{q1})}{2} + j\frac{I_{\mathrm{acq}}G_{\mathrm{id1}}(G_{q1}+G_{p1})}{2} \\ \frac{I_{\mathrm{acd}}G_{\mathrm{id1}}(G_{p1}+G_{q1})}{2} - j\frac{I_{\mathrm{acq}}G_{\mathrm{id1}}(G_{q1}+G_{p1})}{2} & \frac{I_{\mathrm{acd}}G_{\mathrm{id1}}(G_{p1}-G_{q1})}{2} - j\frac{I_{\mathrm{acq}}G_{\mathrm{id1}}(G_{q1}-G_{p1})}{2} \end{bmatrix} \\ & + \frac{G_{\mathrm{PLL}}}{2}\begin{bmatrix} I_{\mathrm{acd}}+jI_{\mathrm{acq}} & -(I_{\mathrm{acd}}+jI_{\mathrm{acq}}) \\ -(I_{\mathrm{acd}}-jI_{\mathrm{acq}}) & I_{\mathrm{acd}}-jI_{\mathrm{acq}} \end{bmatrix} \left\{ \frac{3}{2}\begin{bmatrix} \frac{V_m G_{\mathrm{id1}}(G_{p1}+G_{q1})}{2} & \frac{V_m G_{\mathrm{id1}}(G_{p1}-G_{q1})}{2} \\ \frac{V_m G_{\mathrm{id1}}(G_{p1}-G_{q1})}{2} & \frac{V_m G_{\mathrm{id1}}(G_{p1}+G_{q1})}{2} \end{bmatrix} + \begin{bmatrix} G_{\mathrm{id1}} & \\ & G_{\mathrm{id1}} \end{bmatrix} \right\} \end{aligned} \tag{C.2}$$

APPENDIX C

$\mathbf{H_x}$ and $\mathbf{H_v}$ in (51) are given by (C.1) and (C.2), as shown at the top of this page.

REFERENCES

[1] H. Wu, X. Wang, Ł. Kocewiak, and L. Harnefors, "AC impedance modeling of modular multilevel converters and two-level voltage-source converters: Similarities and differences," in *Proc. IEEE 19th Workshop Control Modeling Power Electron. (COMPEL)*, Jun. 2018, pp. 1–8.

[2] Q. Tu, Z. Xu, and L. Xu, "Reduced switching-frequency modulation and circulating current suppression for modular multilevel converters," *IEEE Trans. Power Del.*, vol. 26, no. 3, pp. 2009–2017, Jul. 2011.

[3] J. Lyu, X. Zhang, X. Cai, and M. Molinas, "Harmonic state-space based small-signal impedance modeling of a modular multilevel converter with consideration of internal harmonic dynamics," *IEEE Trans. Power Electron.*, vol. 34, no. 3, pp. 2134–2148, Mar. 2019.

[4] K. Ji, G. Tang, J. Yang, Y. Li, and D. Liu, "Harmonic stability analysis of MMC-based DC system using DC impedance model," *IEEE J. Emerg. Sel. Topics Power Electron.*, to be published.

[5] Y. Zhou, D. Jiang, J. Guo, P. Hu, and Y. Liang, "Analysis and control of modular multilevel converters under unbalanced conditions," *IEEE Trans. Power Del.*, vol. 28, no. 4, pp. 1986–1995, Oct. 2013.

[6] L. Harnefors, A. Antonopoulos, S. Norrga, L. Ängquist, and H.-P. Nee, "Dynamic analysis of modular multilevel converters," *IEEE Trans. Ind. Electron.*, vol. 60, no. 7, pp. 2526–2537, Jul. 2013.

[7] A. Jamshidifar and D. Jovcic, "Small-signal dynamic DQ model of modular multilevel converter for system studies," *IEEE Trans. Power Del.*, vol. 31, no. 1, pp. 191–199, Feb. 2016.

[8] T. Li, A. M. Gole, and C. Zhao, "Harmonic instability in MMC-HVDC converters resulting from internal dynamics," *IEEE Trans. Power Del.*, vol. 31, no. 4, pp. 1738–1747, Aug. 2016.

[9] J. Freytes *et al.*, "Improving small-signal stability of an MMC with CCSC by control of the internally stored energy," *IEEE Trans. Power Del.*, vol. 33, no. 1, pp. 429–439, Feb. 2018.

[10] Y. Li *et al.*, "Modeling and damping control of modular multilevel converter based DC grid," *IEEE Trans. Power Syst.*, vol. 33, no. 1, pp. 723–735, Jun. 2018.

[11] J.-W. Moon, C.-S. Kim, J.-W. Park, D.-W. Kang, and J.-M. Kim, "Circulating current control in MMC under the unbalanced voltage," *IEEE Trans. Power Del.*, vol. 28, no. 3, pp. 1952–1959, Jul. 2013.

[12] S. Li, X. Wang, Z. Yao, T. Li, and Z. Peng, "Circulating current suppressing strategy for MMC-HVDC based on nonideal proportional resonant controllers under unbalanced grid conditions," *IEEE Trans. Power Electron.*, vol. 30, no. 1, pp. 387–397, Jan. 2015.

[13] H. Wu, X. Wang, and Ł. Kocewiak, "Impedance-based stability analysis of voltage-controlled MMCs feeding linear AC systems," *IEEE J. Emerg. Sel. Topics Power Electron.*, to be published, doi: 10.1109/JESTPE.2019.2911654.

[14] Z. Xu, B. Li, S. Wang, S. Zhang, and D. Xu, "Generalized single-phase harmonic state space modeling of the modular multilevel converter with zero-sequence voltage compensation," *IEEE Trans. Ind. Electron.*, vol. 66, no. 8, pp. 6416–6426, Aug. 2019.

[15] J. Lyu, X. Cai, and M. Molinas, "Optimal design of controller parameters for improving the stability of MMC-HVDC for wind farm integration," *IEEE J. Emerg. Sel. Topics Power Electron.*, vol. 6, no. 1, pp. 40–53, Mar. 2018.

[16] J. Sun and H. Liu, "Sequence impedance modeling of modular multilevel converters," *IEEE J. Emerg. Sel. Topics Power Electron.*, vol. 5, no. 4, pp. 1427–1443, Dec. 2018.

[17] L. Bessegato, L. Harnefors, K. Ilves, and S. Norrga, "A method for the calculation of the AC-side admittance of a modular multilevel converter," *IEEE Trans. Power Electron.*, vol. 34, no. 5, pp. 4161–4172, May 2019.

[18] L. Bessegato, L. Harnefors, K. Ilves, and S. Norrga, "Effects of control on the AC-side admittance of a modular multilevel converter," *IEEE Trans. Power Electron.*, vol. 34, no. 8, pp. 7206–7220, Aug. 2019.

[19] C. Zhang, X. Cai, A. Rygg, and M. Molinas, "Sequence domain SISO equivalent models of a grid-tied voltage source converter system for small-signal stability analysis," *IEEE Trans. Energy Convers.*, vol. 33, no. 2, pp. 741–749, Jun. 2018.

[20] W. Ren and E. Larsen, "A refined frequency scan approach to sub-synchronous control interaction (SSCI) study of wind farms," *IEEE Trans. Power Syst.*, vol. 31, no. 5, pp. 3904–3912, Sep. 2016.

[21] G. C. Paap, "Symmetrical components in the time domain and their application to power network calculations," *IEEE Trans. Power Syst.*, vol. 15, no. 2, pp. 522–528, May 2000.

[22] N. M. Wereley, "Analysis and control of linear periodically time varying systems," Ph.D. dissertation, Dept. Aeronaut. Astronaut., MIT, Cambridge, MA, USA, 1991.

[23] B. Wen, D. Boroyevich, R. Burgos, P. Mattavelli, and Z. Shen, "Analysis of D-Q small-signal impedance of grid-tied inverters," *IEEE Trans. Power Electron.*, vol. 31, no. 1, pp. 675–687, Jan. 2016.

[24] X. Wang, L. Harnefors, and F. Blaabjerg, "Unified impedance model of grid-connected voltage-source converters," *IEEE Trans. Power Electron.*, vol. 33, no. 2, pp. 1775–1787, Feb. 2018.

[25] H. Liu, "HVDC converters impedance modeling and system stability analysis," Ph.D. dissertation, Dept. Elect., Comput., Syst. Eng., Rensselaer Polytech. Inst., Troy, NY, USA, 2017.

[26] K. Sharifabadi, L. Harnefors, H. Nee, S. Norrga, and R. Teodorescu, *Design, Control, and Application of Modular Multilevel Converters for HVDC Transmission Systems*. Hoboken, NJ, USA: Wiley, 2016.

[27] C. Zou *et al.*, "Analysis of resonance between a VSC-HVDC Converter and the AC Grid," *IEEE Trans. Power Electron.*, vol. 33, no. 12, pp. 10157–10168, Dec. 2018.

[28] J. Z. Zhou, D. Hui, S. Fan, Y. Zhang, and A. M. Gole, "Impact of short-circuit ratio and phase-locked-loop parameters on the small-signal behavior of a VSC-HVDC converter," *IEEE Trans. Power Del.*, vol. 29, no. 5, pp. 2287–2296, Oct. 2014.

[29] J. Matevosyan *et al.*, "Grid-forming inverters: Are they the key for high renewable penetration?" *IEEE Power Energy Mag.*, vol. 17, no. 6, pp. 89–98, Nov./Dec. 2019.

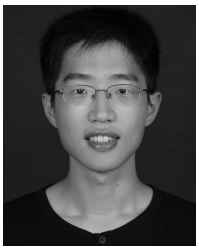

Heng Wu (S'17) received the B.S. and M.S. degrees in electrical engineering from the Nanjing University of Aeronautics and Astronautics (NUAA), Nanjing, China, in 2012 and 2015, respectively. He is currently pursuing the Ph.D. degree in power electronic engineering with Aalborg University, Aalborg, Denmark.

From 2015 to 2017, he was an Electrical Engineer with NR Electric Company, Ltd., Nanjing. He was a Guest Researcher with Ørsted Wind Power, Fredericia, Denmark, from November 2018 to December 2018, and with Bundeswehr University Munich, Neubiberg, Germany, from September 2019 to December 2019. His research interests include the modeling and stability analysis of the power electronic-based power systems.

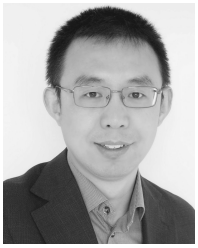

Xiongfei Wang (S'10–M'13–SM'17) received the B.S. degree from Yanshan University, Qinhuangdao, China, in 2006, the M.S. degree from the Harbin Institute of Technology, Harbin, China, in 2008, all in electrical engineering, and the Ph.D. degree in energy technology from Aalborg University, Aalborg, Denmark, in 2013.

Since 2009, he has been with the Department of Energy Technology, Aalborg University, where he became an Assistant Professor in 2014, an Associate Professor in 2016, and a Professor and the Research Program Leader of the Electronic Power Grid (eGrid) in 2018. His current research interests include modeling and control of grid interactive power converters, stability and power quality of power electronic-based power systems, and active and passive filters.

Dr. Wang received six IEEE prize paper awards, the 2016 Outstanding Reviewer Award of the IEEE TRANSACTIONS ON POWER ELECTRONICS, the 2018 IEEE PELS Richard M. Bass Outstanding Young Power Electronics Engineer Award, the 2019 IEEE PELS Sustainable Energy Systems Technical Achievement Award, and the 2019 Highly Cited Researcher in the Web of Science. He serves as an Associate Editor for the IEEE TRANSACTIONS ON POWER ELECTRONICS, the IEEE TRANSACTIONS ON INDUSTRY APPLICATIONS, and the IEEE JOURNAL OF EMERGING AND SELECTED TOPICS IN POWER ELECTRONICS. He was selected into Aalborg University Strategic Talent Management Program in 2016.